The Astrophysical Journal, 1001:79 (21pp), 2026 April 10 https://doi.org/10.3847/1538-4357/ae505e

Chemical Radial Gradients for the Bulge Bar Stellar Populations from the APOGEE Survey

J. V. Sales-Silva[1], K. Cunha[1,2], V. V. Smith[3], S. Daflon[1], D. Souto[4], R. Guerço[1,5], V. Loaiza-Tacuri[4], A. Queiroz[6,7], C. Chiappini[8], I. Minchev[8], S. R. Majewski[9], B. Barbuy[10], D. Bizyaev[11,12], José G. Fernández-Trincado[5,13], Peter M. Frinchaboy[14], S. Hasselquist[15], D. Horta[16], Henrik Jönsson[17], T. Masseron[6,7], N. Prantzos[18], R. P. Schiavon[19], M. Schultheis[20], and M. Zoccali[21]
[1] Observatório Nacional/MCTI, R. Gen. José Cristino, 77, 20921-400, Rio de Janeiro, Brazil; joaovsaless@gmail.com
[2] Steward Observatory, University of Arizona, Tucson, AZ 85719, USA
[3] NOIRLab, Tucson, AZ 85719, USA
[4] Departamento de Física, Universidade Federal de Sergipe, Av. Marechal Rondon, S/N, 49000-000 São Cristóvão, SE, Brazil
[5] Universidad Católica del Norte, Núcleo UCN en Arqueología Galáctica—Inst. de Astronomía, Av. Angamos 0610, Antofagasta, Chile
[6] Instituto de Astrofísica de Canarias (IAC), E-38205 La Laguna, Tenerife, Spain
[7] Universidad de La Laguna (ULL), Departamento de Astrofísica, 38206, La Laguna, Tenerife, Spain
[8] Leibniz-Institut für Astrophysik Potsdam (AIP), An der Sternwarte 16, 14482 Potsdam, Germany
[9] Department of Astronomy, University of Virginia, Charlottesville, VA 22904-4325, USA
[10] Universidade de São Paulo, IAG, Rua do Matão 1226, Cidade Universitária, São Paulo 05508-090, Brazil
[11] Apache Point Observatory and New Mexico State University, P.O. Box 59, Sunspot, NM 88349-0059, USA
[12] Sternberg Astronomical Institute, Moscow State University, Moscow, Russia
[13] Universidad Católica del Norte, Departamento de Ingeniería de Sistemas y Computación, Av. Angamos 0610, Antofagasta, Chile
[14] Department of Physics and Astronomy, Texas Christian University, TCU Box 298840, Fort Worth, TX 76129, USA
[15] Space Telescope Science Institute, Baltimore, MD, USA
[16] Institute for Astronomy, University of Edinburgh, Royal Observatory, Blackford Hill, Edinburgh EH9 3HJ, UK
[17] Materials Science and Applied Mathematics, Malmö University, SE-205 06 Malmö, Sweden
[18] Institute d'Astrophysique de Paris, UMR 7095 CNRS & Sorbonne Université, 98 bis Boulevard, Arago, Paris 75014, France
[19] Astrophysics Research Institute, Liverpool John Moores University, Liverpool, L3 5RF, UK
[20] Université Côte d'Azur, Observatoire de la Côte d'Azur, CNRS, Laboratoire Lagrange, Bd de l'Observatoire, CS 34229, 06304, Nice Cedex 4, France
[21] Instituto de Astrofísica, Pontificia Universidad Católica de Chile, Vicuñ Mackenna 4860, Macul, Casilla 306, Santiago 22, Chile
Received 2025 October 15; revised 2026 February 19; accepted 2026 March 9; published 2026 April 6

Abstract

The Milky Way bulge bar is composed of multiple populations. Using chemical and kinematical planes, we segregate six populations in a bulge bar sample observed by the APOGEE survey: two with bar-driven orbits, two with eccentric orbits, and two with low-eccentricity orbits, each composed of low- and high-[Mg/Fe] stars. Our sample spans $-2.0 \lesssim$ [Fe/H] $\lesssim +0.5$ and Galactocentric distance $R_{\rm Gal} < 6$ kpc. We use chemical abundances from APOGEE DR17 for the elements Mg, Si, Ca, Al, K, Mn, Co, Ni, and Fe and from the BAWLAS catalog for Ce and Nd. We find that the low- and high-[Mg/Fe] stars with low-eccentricity orbits, which exhibit chemical and orbital characteristics similar to those of the low- and high-[α/Fe] disks, display slightly negative and positive metallicity gradients, respectively. This result for the low-[Mg/Fe], low-eccentricity stars indicates a break in the global thin-disk metallicity gradient. The high-eccentricity populations with both low and high [Mg/Fe] show approximately flat metallicity gradients. In general, the [X/H] gradients of all elements for all populations follow Fe, except for the neutron-capture elements Ce and Nd. For all elements, the high-[Mg/Fe] bar population shows a much steeper positive [X/H] gradient than the nearly flat gradient for the low-[Mg/Fe] bar stars. The positive [X/H] gradients observed among our high-[Mg/Fe] bar stars probably reflect an age variation along the peanut structure. This interpretation agrees with the *N*-body simulations. Such steep positive gradients have also been reported in some high-redshift ($z \sim 4$–10) galaxies.

Unified Astronomy Thesaurus concepts: Milky Way Galaxy (1054); Galactic bulge (2041); Stellar populations (1622); Stellar abundances (1577); Stellar kinematics (1608)

1. Introduction

The distribution of metals in the Milky Way (MW) reflects the history of the Galaxy's formation and evolution, as shaped by the processes of our Galaxy's interactions (e.g., accretion), stellar migration, star formation, stellar nucleosynthetic yields, and gas flows. This panorama places chemical abundance gradients as valuable observable constraints on models of the MW's chemical evolution.

Radial abundance trends of the thin disk are well established in the literature through the analysis of open clusters (e.g., L. Magrini et al. 2023; J. Carbajo-Hijarrubia et al. 2024; M. Palla et al. 2024; J. M. Otto et al. 2026), Cepheids (e.g., K. Genovali et al. 2014; R. da Silva et al. 2023), and field stars (e.g., OB stars, S. Daflon & K. Cunha 2004; G. A. Bragança et al. 2019; red giants, F. Anders et al. 2017; J. W. Johnson et al. 2025; planetary nebulae, L. Stanghellini & M. Haywood 2018), with the radial metallicity gradient of the thin disk varying roughly between ~ -0.02 and ~ -0.08 dex kpc^{-1}, depending on the sample and population analyzed. Different types of objects or populations probe distinct gradient epochs from Galaxy formation. Models from I. Minchev et al. (2018)

find that the interstellar medium (ISM) radial metallicity gradient is steeper at the time of disk formation and flattens as the Galaxy evolves. The negative value for the thin-disk metallicity gradient corroborates an inside-out disk formation scenario (where the innermost regions are assumed to have formed faster than the outermost ones) adopted in chemical evolution models (e.g., C. Chiappini et al. 2001; M. Kubryk et al. 2015; R. Schönrich & P. J. McMillan 2017; N. Frankel et al. 2019; N. Prantzos et al. 2023). On the other hand, the thick-disk stellar population (morphologically defined[22]) shows a flat radial metallicity trend (e.g., J. Y. Cheng et al. 2012; A.-C. Eilers et al. 2022), or inverted and positive (e.g., K. Carrell et al. 2012; F. Anders et al. 2014; M. R. Hayden et al. 2014; W. Sun et al. 2024), as seen also in chemodynamical simulations (e.g., I. Minchev et al. 2014; M. S. Miranda et al. 2016; C. Li & G. Zhao 2017). This gradient may represent a turbulent thick-disk formation characterized by intense star formation and is consistent with the radial migration of old thick-disk stars (J. Y. Cheng et al. 2012). In particular, using APOGEE DR16 red giant branch stars, A.-C. Eilers et al. (2022) investigated the radial chemical gradient in the low- and high-α populations from the disk for 20 chemical species, including the inner region of the Galaxy. They found no chemical gradients for high-α stars, no abundance variations due to bar, and that the radial metallicity gradient from the inner Galaxy is negative and varies continuously in the low-α population. Additionally, B. L. Ratcliffe & M. K. Ness (2023) analyzed the gradient in low- and high-α disk populations in bins of ([Fe/H], [Mg/Fe]), finding near-zero slopes for many [X/Fe] ratios, such as for Al, alpha, and iron-peak elements. In the extragalactic context, metal radial gradients have been observed in most disk galaxies, indicating that abundances decrease outward and may also flatten over time (e.g., Z. Li et al. 2025). Positive gradients have also been observed in some galaxies (e.g., P. Troncoso et al. 2014; X. Wang et al. 2022).

A bar with a boxy/peanut morphology and an X-shaped structure (e.g., A. McWilliam & M. Zoccali 2010; C. Wegg & O. Gerhard 2013; M. Ness & D. Lang 2016; M. Zoccali et al. 2017) characterizes the bulge of the MW, composed of stars spanning a broad metallicity range ($-1.5 < [\mathrm{Fe/H}] < 0.5$; B. Barbuy et al. 2018) and mostly old (with possibly only a small fraction of the more metal-rich stars being younger than 5 Gyr; T. Bensby et al. 2017). Like the local disk, the MW bulge also features stars with high and low [α/Fe] ratios (e.g., A. Rojas-Arriagada et al. 2019; A. B. A. Queiroz et al. 2020, 2021). Observations of its stellar populations and Galactic evolutionary models posit the formation of the MW bulge as a combination of violent, early-Universe processes such as accretion of small Galactic fragments (imprinted in the classical spheroidal bulge component) and dynamical secular evolution of the disk (traced by the pseudo–bar-boxy-peanut component).

In general, the radial abundance gradients for stellar populations in the inner Galaxy ($R_{\mathrm{Gal}} < 5$ kpc) are still little explored, and literature results are generally limited to the analysis of Fe and α-elements (e.g., D. Minniti et al. 1995; S. J. Smartt et al. 2001; R. M. Rich et al. 2007; M. Zoccali et al. 2008; O. A. Gonzalez et al. 2013; A. B. A. Queiroz et al. 2021), indicating that in regions closer to the Galactic center the stars are more metal-poor or metal-rich depending on whether the sample is near or far from the Galactic plane (A. B. A. Queiroz et al. 2020, 2021). Probing chemical gradients in the inner Galaxy is challenging, in part due to high extinction caused by the dust present in this region, but also due to crowded fields. In addition, fields are composed of a complex mixture of stellar populations: stars from the bulge bar, in situ disk stars, or disk stars that were born outside the bulge region but have migrated inward, the halo passing through the inner region, globular and open clusters (or lost stars from these clusters, such as N-rich stars), and stars accreted by our Galaxy and located in the central region (e.g., stars from Heracles; D. Horta et al. 2021). The high extinction present in the inner Galaxy limits optical observations to a few windows, such as Baade's window (e.g., A. McWilliam & R. M. Rich 1994; K. Cunha & V. V. Smith 2006; V. Hill et al. 2011), or well above the plane (e.g., F. Sestito et al. 2023). In recent years, with the advent of Gaia and the availability of high-resolution near-infrared spectra, detailed multidimensional (chemical, positional, and kinematic) analyses of stars in the inner Galaxy have become possible (e.g., A. E. García Pérez et al. 2018; J. G. Fernández-Trincado et al. 2019; A. Rojas-Arriagada et al. 2019; G. Zasowski et al. 2019; A. B. A. Queiroz et al. 2021; S. Khoperskov et al. 2025; S. Nepal et al. 2025). Using Gaia astrometric data and the high-resolution spectroscopic survey the Apache Point Observatory Galactic Evolution Experiment (APOGEE; S. R. Majewski et al. 2017) in the H band (1.514–1.696 μm), S. Khoperskov et al. (2025) found that there is no universal metallicity gradient for the bulge of the MW. To understand the formation of the inner MW and its multiple populations more fully, it is essential to analyze the specific chemical gradients of each population separated via a chemodynamical analysis.

Using APOGEE data, A. B. A. Queiroz et al. (2021) performed a detailed orbital-chemical analysis of the stellar populations in the Galactic bulge bar, segregating the different populations: stars from the bar, from the spheroidal pressure-supported bulge component, and from the inner thin and inner thick disk. This allowed, for example, the discovery that the stellar population with a high probability of being in the boxy-peanut bulge is composed of stars with high and low [α/Fe] ratios (A. B. A. Queiroz et al. 2021).

Based on the sample of A. B. A. Queiroz et al. (2021) of the Galactic bulge bar, in this study we estimate the radial gradients in the different populations in the inner Galaxy for the α-elements Mg, Si, and Ca; the odd-Z elements Al and K; the Fe-peak elements Mn, Co, Ni, and Fe; and the heavy elements Ce and Nd. Studying the radial gradients for distinct elements will reveal their sensitivity to the different timescales of element production and to variation in star formation histories. In Section 2 of this paper, we detail the sample and the methodologies adopted to determine the abundances. The chemo-kinematical segregation of the bulge bar populations is discussed in Section 3. Subsequently (Section 4), we show the chemical gradient for the main populations present in our sample and discuss our findings, comparing them with the gradient from distinct populations and analyzing Galactic evolution scenarios that fit our results. Concluding remarks on our results are found in Section 5.

[22] The thick disk can be defined in different ways: morphologically through decomposition of vertical density profiles or at a fixed height above the disk midplane, kinematically, chemically (high-α sequence), or as the old part of the disk. For a detailed discussion of the different definitions of the thick disk, see M. Martig et al. (2016).

2. Sample and Chemical Abundances

We estimated the radial gradients for the bulge bar stellar populations using the chemical abundances from Data Release 17 (DR17; Abdurro'uf et al. 2022) of the APOGEE survey (S. R. Majewski et al. 2017), which provides the analysis of high-resolution spectra ($R \sim 22{,}500$) in the near-IR (1.514–1.696 μm; J. C. Wilson et al. 2019) for 650,000 stars. APOGEE observations were carried out in both hemispheres, using the 2.5 and 1.0 m telescopes at Apache Point Observatory (New Mexico, USA; J. E. Gunn et al. 2006; J. A. Holtzman et al. 2010) and the 2.5 m Irenee Du Pont telescope at Las Campanas Observatory (La Serena, Chile; I. S. Bowen & A. H. J. Vaughan 1973). D. L. Nidever et al. (2015) and Abdurro'uf et al. (2022) described the APOGEE data reduction pipeline. The APOGEE Stellar Parameters and Chemical Abundance Pipeline (ASPCAP; A. E. García Pérez et al. 2016) and the APOGEE line list (V. V. Smith et al. 2021) were used to determine the chemical abundances and atmospheric parameters in DR17. In this study, we used the chemical abundances of Mg, Si, Ca, Al, K, Mn, Co, Ni, and Fe from DR17 to estimate the gradients.

We also analyzed the neutron-capture elements Ce and Nd. In the APOGEE spectra, these elements have weak absorption lines of Ce II and Nd II that overlap with other spectral lines (S. Hasselquist et al. 2016; K. Cunha et al. 2017), hindering the performance of the ASPCAP pipeline in estimating their abundances. We used the Ce and Nd abundances from the BACCHUS Analysis of Weak Lines in the APOGEE (BAWLAS) catalog (C. R. Hayes et al. 2022), which carefully reanalyzed the APOGEE spectra to estimate precise abundances for these elements using the BACCHUS code (T. Masseron et al. 2016). However, the BAWLAS sample is restricted to APOGEE red giants having calibrated ASPCAP stellar parameters of 3500 K $< T_{\rm eff} <$ 5000 K and $\log g < 3.5$ and high signal-to-noise ratio (S/N) spectra (S/N > 150).

We used the bulge bar sample from A. B. A. Queiroz et al. (2021), as done by J. V. Sales-Silva et al. (2024) in the Ce and Nd analysis for the bulge bar stars. A. B. A. Queiroz et al. (2021) selected only stars with high S/N (>50) and an excellent spectrum fit using the ASPCAP pipeline (ASPCAP_CHI2<25). A. B. A. Queiroz et al. (2021) utilized a Bayesian tool, StarHorse (B. X. Santiago et al. 2016; A. B. A. Queiroz et al. 2018), to derive distances, extinctions, and other astrophysical parameters of stars based on APOGEE, Gaia, and photometric (Two Micron All Sky Survey, Pan-STARRS1, and AllWISE) data. This analysis allowed access to the 6D phase space of the APOGEE stars with excellent precision, with an uncertainty of around 7% in distance. With this mapping, A. B. A. Queiroz et al. (2021) selected 26,500 stars in the central region of the Galaxy with Galactocentric Cartesian coordinates contained within $|X_{\rm Gal}| < 5$ kpc, $|Y_{\rm Gal}| < 3.5$ kpc, and $|Z_{\rm Gal}| < 1.0$ kpc. To clean the bulge bar sample of the most apparent disk and halo stars, Queiroz et al. used the reduced proper-motion diagram, a tool to segregate distinct kinematical populations (e.g., L. T. G. Chiu 1980; J. K. Faherty et al. 2009; M. C. Smith et al. 2009), and found ~8000 stars that belong to the Galactic bulge bar. In this study, using this cleaned bulge bar sample, we analyze the radial chemical abundance gradients of the following elements: Mg, Si, Ca, Al, K, Mn, Co, Ni, and Fe. We then cross-correlate this sample with the BAWLAS catalog, resulting in a sample of 2098 stars with which we investigate radial gradients of the elements Ce and Nd.

The mean errors and their respective standard deviations of the atmospheric parameters for our sample are $\sigma_{\log g} = 0.03 \pm 0.01$, $\sigma_{T_{\rm eff}} = 7 \pm 2$ K, and $\sigma_{\rm [Fe/H]} = 0.011 \pm 0.002$. The average uncertainties of the abundances of the other elements are $\sigma_{\rm Mg} = 0.015 \pm 0.004$, $\sigma_{\rm Si} = 0.018 \pm 0.005$, $\sigma_{\rm Ca} = 0.018 \pm 0.006$, $\sigma_{\rm Al} = 0.031 \pm 0.008$, $\sigma_{K} = 0.046 \pm 0.011$, $\sigma_{\rm Mn} = 0.020 \pm 0.007$, $\sigma_{\rm Co} = 0.051 \pm 0.026$, $\sigma_{\rm Ni} = 0.017 \pm 0.006$, $\sigma_{\rm Ce} = 0.064 \pm 0.034$, and $\sigma_{\rm Nd} = 0.087 \pm 0.051$.

We investigate the potential systematic effects of atmospheric parameters on the chemical abundances of DR17. Our sample comprises giant stars ($0.0 < \log g < 3.0$), with the bulk of the $\log g$ values between 0.5 and 2.5. The selection of red giants displays only minor trends in both $T_{\rm eff}$ and $\log g$ as functions of $R_{\rm Gal}$, partially due to our rather restricted ranges in Galactocentric distance ($R_{\rm Gal} \approx$ 0–5 kpc) and longitude toward the Galactic center. We also select only elements with high-precision measurements for giants in DR17 that follow the trends expected from the literature. Our sample constraints, with restricted atmospheric parameters and precise abundance estimates, reduce the effect of atmospheric parameter systematics on both the DR17 abundances and the resulting abundance gradient estimates. Furthermore, potential concerns about empirical abundance corrections (e.g., A.-C. Eilers et al. 2022; T. Sit et al. 2024) are mitigated by the absence of a strong correlation between $\log g$, distance, and abundances in our sample.

3. Chemo-kinematical Segregation of the Bulge Bar Populations

The inner Galaxy is known to be composed of multiple populations, as indicated by the multipeaked metallicity distribution function in the bulge (e.g., M. Ness et al. 2013; A. Rojas-Arriagada et al. 2017; M. Zoccali et al. 2017; C. I. Johnson et al. 2022). Recently, S. Nepal et al. (2025) revealed some characteristics of the different populations present in the inner region of the Galaxy using data from A. B. A. Queiroz et al. (2021) and from the Gaia DR3 Radial Velocity Spectrograph. For example, S. Nepal et al. (2025) found that the metallicity distribution of the bulge spheroidal population peaks at around −0.7 dex and is dominated by a high-[α/Fe] population. We separated the populations in the inner MW by using chemical planes and kinematical decomposition within the $|Z_{\rm max}|$–ecc plane, but we also investigated the presence of known stellar populations in our sample using literature catalogs of chemically peculiar stars (N-rich stars), globular cluster (GC) stars (E. Vasiliev & H. Baumgardt 2021; R. P. Schiavon et al. 2024), and possibly ex situ stars (D. Horta et al. 2021; S. Nepal et al. 2025), as done in J. V. Sales-Silva et al. (2024).

First, we analyzed the presence of GC stars within our bulge bar sample using catalogs of E. Vasiliev & H. Baumgardt (2021) and R. P. Schiavon et al. (2024). E. Vasiliev & H. Baumgardt (2021) cataloged the probable member stars of 170 GCs using data from Gaia Early Data Release 3 (EDR3), while R. P. Schiavon et al. (2024) cataloged the stars of all known Galactic GCs observed by APOGEE in DR17 based on position, proper motion, and radial velocity. We cross-matched the probable members ($P > 0.7$) of the GCs from both of these catalogs against our reduced-proper-motion-diagram-segregated bulge bar sample and found 37 stars that are possible

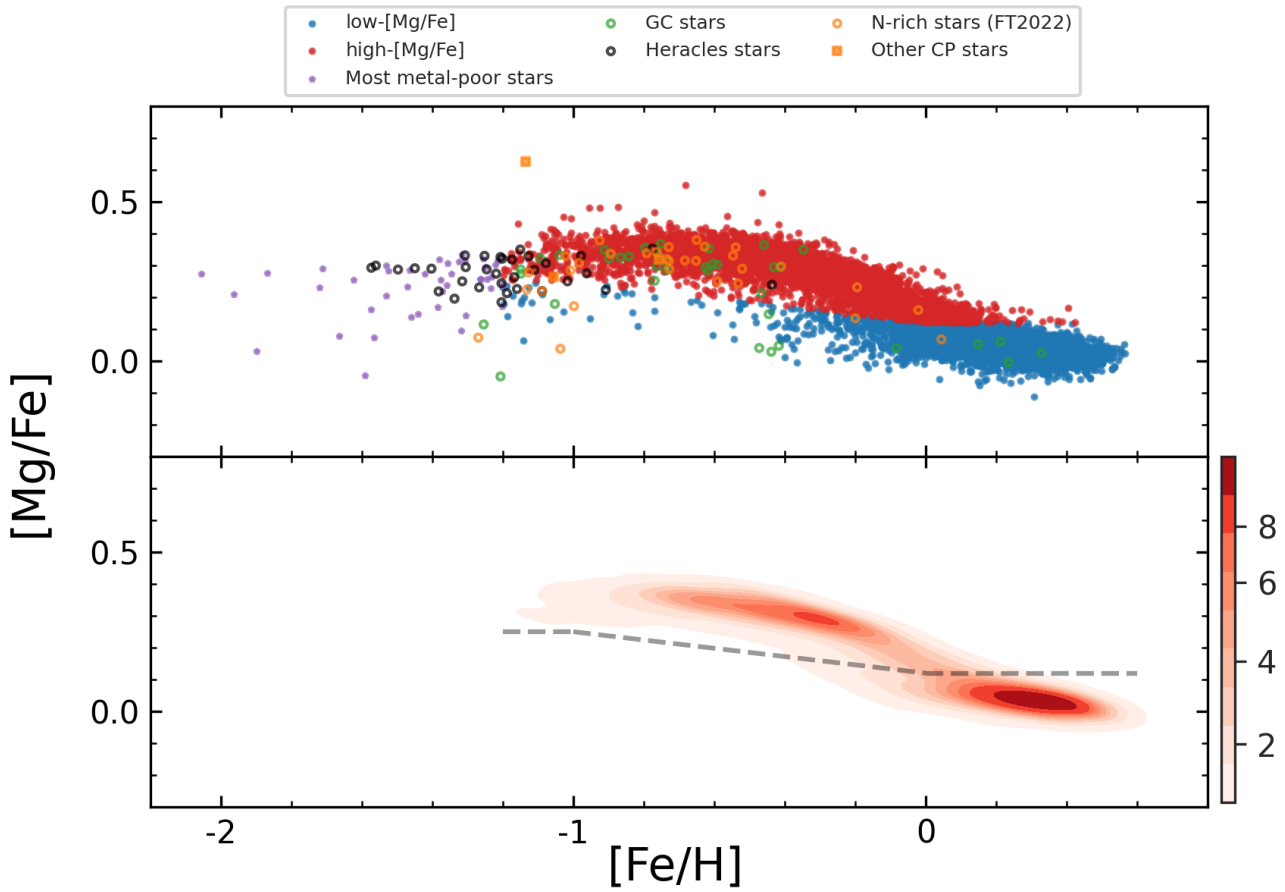

Figure 1. The [Mg/Fe]–[Fe/H] plane for the studied inner Galaxy sample. The top panel shows the low-[Mg/Fe] sequence in blue and the high-[Mg/Fe] sequence in red. Stars from our sample that have been identified as being from GCs, members of the Heracles substructure, N-rich, or chemically peculiar are marked with different symbols. The most metal-poor stars are also marked. The bottom panel shows the relative density distribution in this chemical plane, color-coded according to the probability density function. The dashed line separates the low- and high-[Mg/Fe] populations, as described in the text.

members of GCs. We also investigated the presence of N-rich stars, a chemically peculiar population known to be present in the inner Galaxy. J. G. Fernández-Trincado et al. (2022, hereafter FT2022) provided a catalog containing 412 N-rich stars in the APOGEE survey, 34 of which are in our sample. We also separated the three chemically peculiar stars detected in J. V. Sales-Silva et al. (2024) that are not in the FT2022 sample. Finally, we found 33 stars within our bulge bar sample that belonged to the Heracles substructure, from cross-matching our bulge bar sample with the Heracles stars in D. Horta et al. (2021). In addition, as in our previous study (J. V. Sales-Silva et al. 2024), we consider stars with [Fe/H] < -1.2 as a separate bulge bar population, naming these stars as the most metal-poor bulge bar stars, which are likely related to the inner stellar halo or protogalactic population (H.-W. Rix et al. 2022; A. Ardern-Arentsen et al. 2024; S. Nepal et al. 2025).

In Figure 1 we segregate the low- and high-[Mg/Fe] bulge bar populations, using the same criteria as in J. V. Sales-Silva et al. (2024). Looking at the density distribution (bottom panel of Figure 1), two sequences stand out in the [Mg/Fe]–[Fe/H] plane: one population centered close to solar [Mg/Fe] values ($\sim$0.05 dex) and high [Fe/H] ($\sim$0.3 dex), and the other with high [Mg/Fe] ratios and low [Fe/H]. From now on, we designate these two sequences as the low-[Mg/Fe] and high-[Mg/Fe] populations. The dashed line in the bottom panel of Figure 1 (taken from J. V. Sales-Silva et al. 2024) was used to segregate the high- and low- Mg/Fe populations. The blue and red circles in the top panel of Figure 1 represent the stars in the low- and high-[Mg/Fe] populations in our sample, respectively. The stars from GCs and the chemically peculiar, most metal-poor, and Heracles substructure stars discussed above are marked with different symbols in Figure 1.

We also detected the presence of other stellar populations in our sample by analyzing other chemical planes. In Figure 2, we show the [X/Fe]–[Fe/H] planes for Al, K, and Ni, for the high-[Mg/Fe] (shown in red) and low-[Mg/Fe] (shown in blue) populations. We find evidence for the presence of other populations within the sample of stars with low [Mg/Fe] and [Fe/H] > -0.8 (blue distributions). We identify two clumps in the density distribution of the low-[Mg/Fe] population (middle panels) and multiple peaks in the histograms (right panels) in the chemical planes of the three elements. One of the populations has stars with low [Al/Fe] ratios ([Al/Fe] < -0.13), similar to the old and accreted stars found in the MW disk by D. K. Feuillet et al. (2022). We find that these Al-poor stars have mostly eccentric orbits ($\langle ecc_{Alpoor} \rangle = 0.76 \pm 0.16$), which corroborates with their extragalactic nature. The discovery of these stars in the inner region contributes to the mapping and characterization of this accretion event.

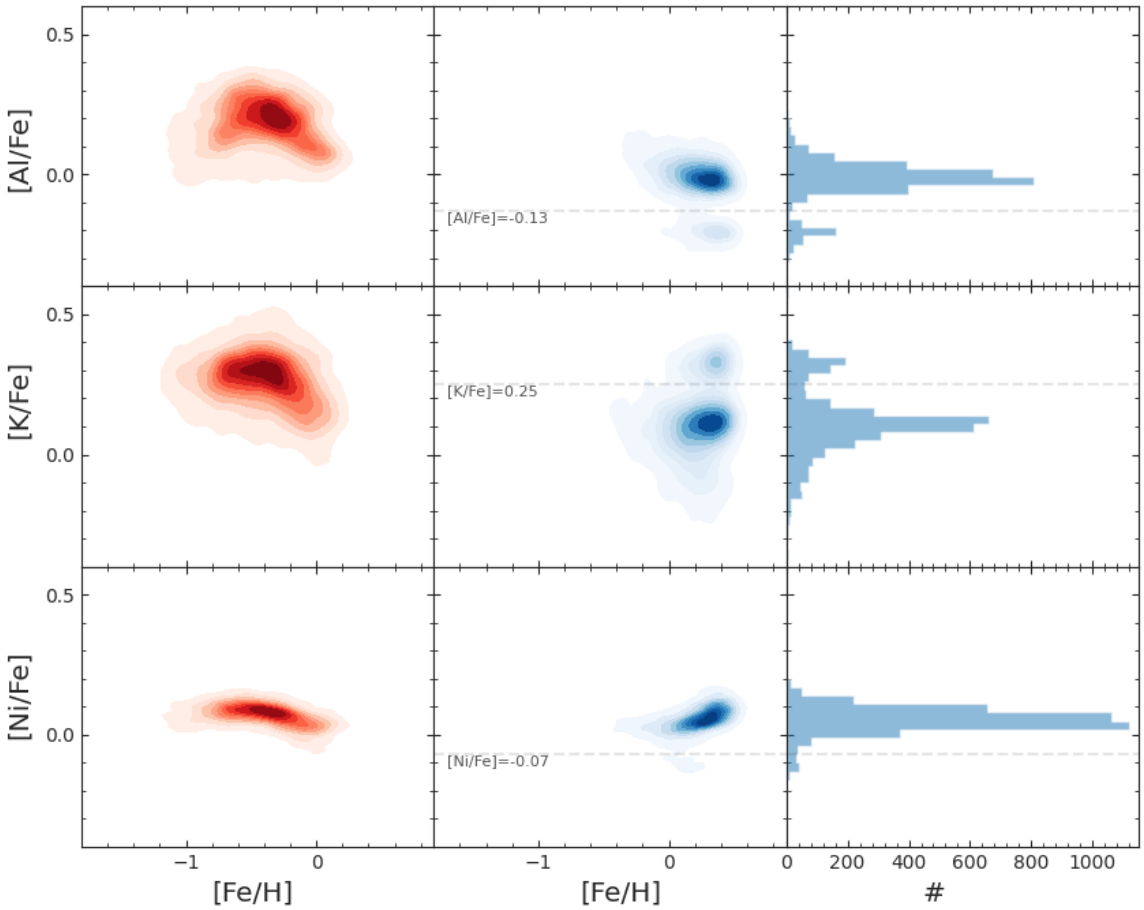

Figure 2. Distribution for the elements Al, K, and Ni, color-coded according to the probability density function. The left and middle panels show the red and blue distributions for the high- and low-[Mg/Fe] populations, respectively. The dashed lines in the middle panels separate the multiple chemical populations of the low-[Mg/Fe] bulge bar stars. The right panels present the histogram for the low-[Mg/Fe] stars.

We also identified K-rich stars ([K/Fe] > 0.25) in the population of low-[Mg/Fe] stars. Unlike C, N, and Na, changes in K abundances are not expected to be due to dredge-up, and stellar evolution cannot explain the K enrichment in the red giant stars. A. J. Kemp et al. (2018) found 112 K-rich stars mining LAMOST data of ∼500,000 MW field stars and hypothesized that a super–asymptotic giant branch binary system may produce this peculiar chemical signature. In addition, some stars in GCs may exhibit an enrichment in potassium (e.g., D. A. Alvarez Garay et al. 2022), and these stars with high [K/Fe] ratios in the inner Galaxy might be lost stars from GCs, similar to the N-rich stars. However, a complication for this scenario is that these stars are not metal-poor, generally presenting [Fe/H] > 0.0. The chemical peculiarity of K-rich stars may be due to stellar outflows from the super–asymptotic giant branch (P. Ventura et al. 2012), or pair-instability supernovae (E. Carretta et al. 2013), which can pollute the stellar atmospheres in dense stellar environments like the bulge. However, N. Prantzos et al. (2017) found that the enrichment of K in K-rich stars from GCs cannot be explained by the material produced by super-AGBs. In fact, the origin of K-rich stars is currently poorly understood.

In the [Ni/Fe]–[Fe/H] plane of the low-[Mg/Fe] population (shown in the bottom panel of Figure 2), there is a small collection of stars with low [Ni/Fe] ([Ni/Fe] < –0.07), which is much less prominent than those found for [Al/Fe] and [K/Fe]. Ni is an element of the Fe peak and is mainly ejected into the ISM by Type Ia supernovae (e.g., K. Iwamoto et al. 1999; C. Kobayashi et al. 2006). The characteristics of the progenitors (e.g., white dwarf mass or double-degenerate white dwarf merger) of these supernovae characterize the yields of these events, including the [Ni/Fe] ratio (e.g., I. R. Seitenzahl et al. 2013). Dwarf satellite galaxies contain Ni-poor stars (e.g., A. McWilliam et al. 2018; E. N. Kirby et al. 2019; J. Montalbán et al. 2021). In particular, the Sagittarius dwarf galaxy shows Ni-poor stars with metallicity similar to the Ni-poor stars detected here (see Figure 5 in A. Minelli et al. 2021).

In summary, to analyze the chemical abundance gradient, we removed from the low-[Mg/Fe] population the stars that presented some chemical peculiarities (low [Al/Fe], low [Ni/Fe], or high [K/Fe]) since such chemical signatures may contaminate the study of chemical gradients. In total, we removed 308, 80, and 535 stars from the low-[Al/Fe], low-[Ni/Fe], and high-[K/Fe] regimes, respectively. It is beyond the scope of this paper to discuss further the nature of these chemically peculiar stars in the inner MW, which we intend to do in a future study.

In addition to chemistry, we also used the plane defined by the orbital parameters $|Z_{max}|$ and ecc to characterize the main populations of the bulge bar, where $|Z_{max}|$ is the maximum vertical excursion from the Galactic midplane and ecc is the

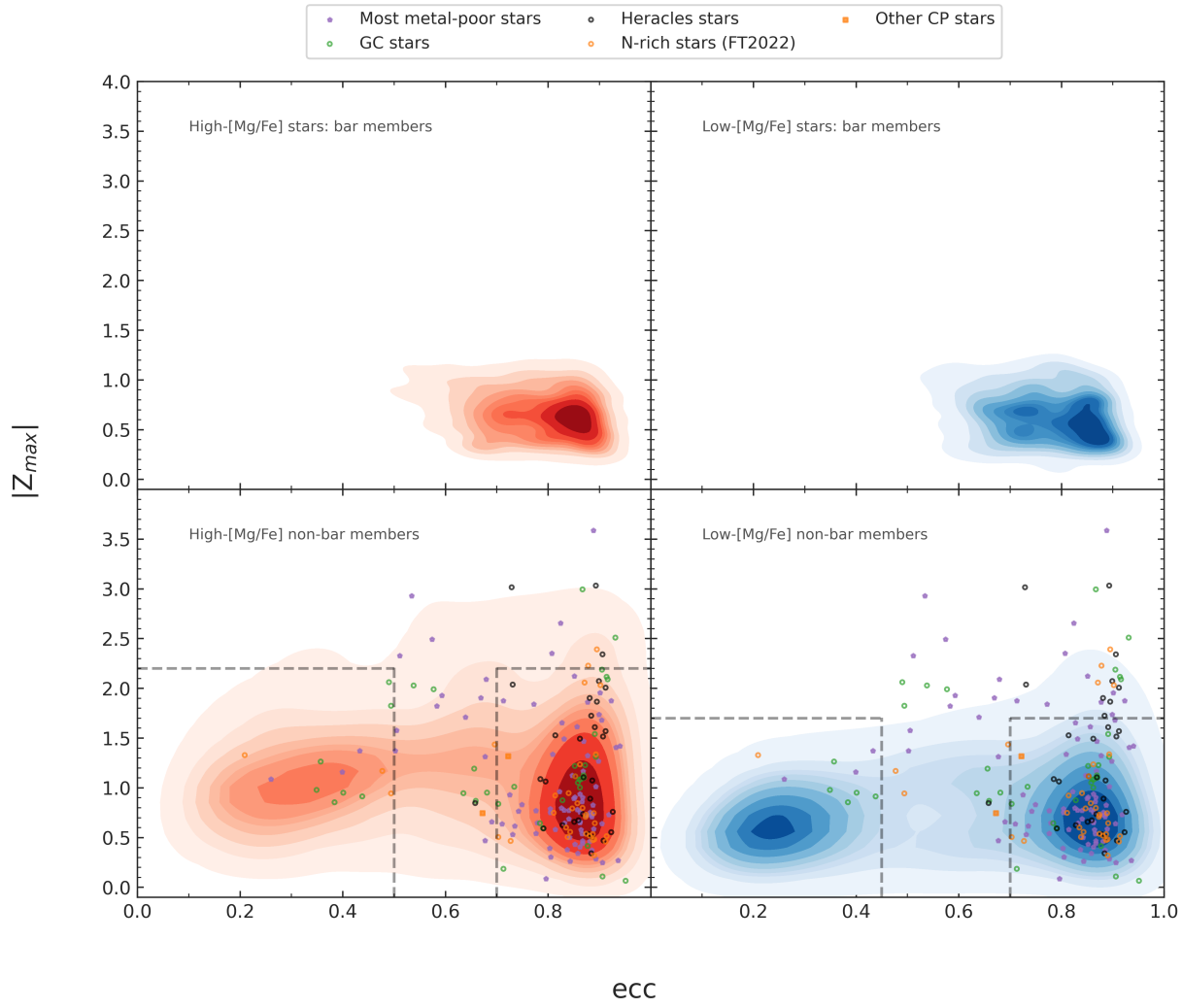

Figure 3. $|Z_{\rm max}|$–eccentricity plane for the bulge bar sample. Top panels relate to the low-[Mg/Fe] (right) and high-[Mg/Fe] (left) bar member stars, and the bottom panels are for the low-[Mg/Fe] (right) and high-[Mg/Fe] (left) stars in the inner Galaxy non-bar-member stars. The dashed lines limit the high- and low-eccentricity populations for the low-[Mg/Fe] (right) and high-[Mg/Fe] (left) stars. Other stars not included in the bulge bar sample (GCs, Heracles, chemically peculiar, and most metal-poor stars) are shown as filled and open symbols.

orbital eccentricity (ecc $= (R_{\rm apo} - R_{\rm peri})/(R_{\rm apo} + R_{\rm peri})$, where $R_{\rm peri}$ is the perigalactic distance and $R_{\rm apo}$ is the apogalactic distance). The $|Z_{\rm max}|$–ecc plane is a useful tool in the study and segregation of stellar populations (e.g., O. J. Eggen et al. 1962; C. Boeche et al. 2013; M. Steinmetz et al. 2020; A. B. A. Queiroz et al. 2021; S. Nepal et al. 2025). A. B. A. Queiroz et al. (2021) estimated the orbital parameters (including $|Z_{\rm max}|$ and ecc) for all stars in our sample, and these are used here to segregate the stellar populations. Details of the method, including the Galactic potential used to calculate the orbital parameters, are described in Section 3 of A. B. A. Queiroz et al. (2021). The standard error of the orbital parameters of our sample is presented in Figure 2 of A. B. A. Queiroz et al. (2021). Overall, the eccentricity error is less than 0.02, while the $Z_{\rm max}$ error is less than 0.10 kpc.

In Figure 3, we plot the density distribution of our sample in the $|Z_{\rm max}|$–ecc plane. Using a kinematical analysis, A. B. A. Queiroz et al. (2021) estimated the probability of stars belonging to the Galactic bar; here we assume that stars with a probability greater than 0.5 are from the bar or have bar-driven orbits. In the top panels of Figure 3, we show the density distributions for the stars of the bar with high (left panel) and low (right panel) [Mg/Fe] ratios. Both of these bar populations are located mainly near the plane $|Z_{\rm max}| \leqslant 1$ kpc, and they have $R_{\rm Gal} \leqslant 2.5$ kpc. In general, bar stars also have orbits with ecc $\gtrapprox 0.55$, and most of these have very high eccentricity (ecc $\gtrsim 0.8$), as expected for bar stars.

In the bottom panels of Figure 3, we show the density distributions in the $|Z_{\rm max}|$–ecc plane for the high- and low-[Mg/Fe] stars that are not considered to be part of the bar. Clearly, the density distributions for both [Mg/Fe] chemical populations show two denser regions. For low-[Mg/Fe] stars, these regions are centered at $|Z_{\rm max}| \approx 0.6$ kpc and ecc ≈ 0.3 and at $|Z_{\rm max}| \approx 0.6$ kpc and ecc ≈ 0.9. For high-[Mg/Fe] stars, the densest regions are centered at $|Z_{\rm max}| \approx 1.0$ kpc and ecc ≈ 0.32 and at $|Z_{\rm max}| \approx 0.9$ kpc and ecc ≈ 0.9. To isolate these main populations, we use limits as indicated by the dashed lines in the figure. We limit the sample of low- and high-[Mg/Fe] stars to $|Z_{\rm max}| < 1.7$ kpc and $|Z_{\rm max}| < 2.2$ kpc, respectively. In addition, we separate stars with low and high eccentricity in both [Mg/Fe] populations. For low-[Mg/Fe] stars, we select stars with ecc lower than 0.45 and higher than 0.7. Meanwhile, the populations of high-[Mg/Fe] stars are selected using ecc lower than 0.50 and higher than 0.75.

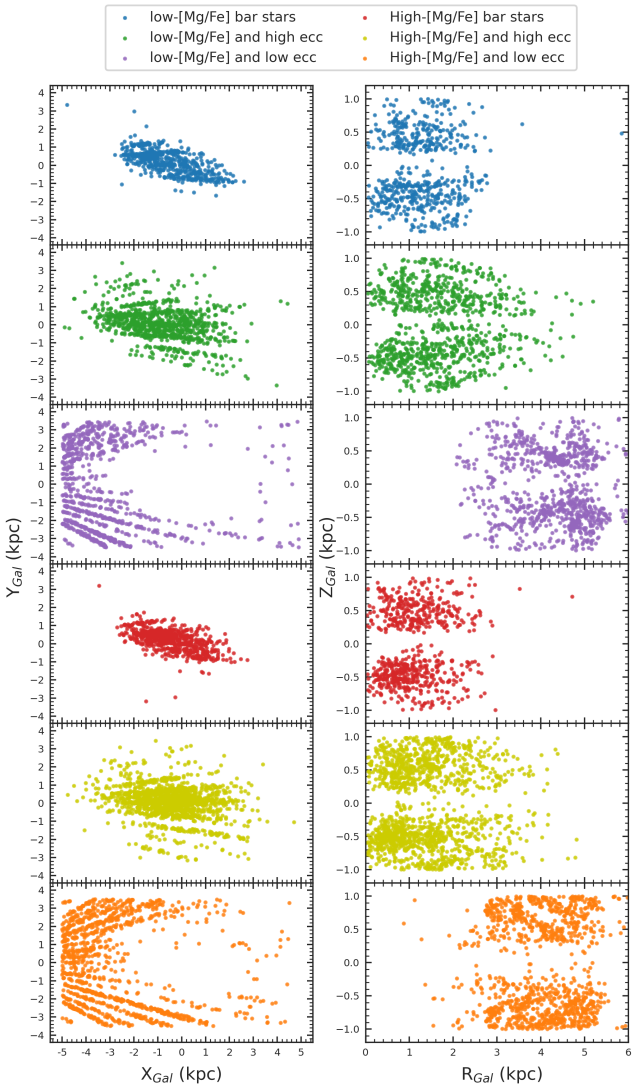

Figure 4. Distribution of six stellar populations present in our sample in the $X_{\rm Gal}$–$Y_{\rm Gal}$ (left panels) and $R_{\rm Gal}$–$Z_{\rm Gal}$ (right panels) planes. Different point colors characterize distinct populations. Blue, green, and purple points represent the low-[Mg/Fe] bar stars, the low-[Mg/Fe] and high-eccentricity population, and the low-[Mg/Fe] and low-eccentricity population, respectively, while red, dark yellow, and orange represent the high-[Mg/Fe] bar stars, the high-[Mg/Fe] and high-eccentricity population, and the high-[Mg/Fe] and low-eccentricity population, respectively.

Summarizing, we chemo-kinematically segregated our inner Galaxy sample into six main populations: two with bar-driven orbits, two with high-eccentricity but non-bar-driven orbits, and two with low-eccentricity orbits, and each pair composed of stars with low and high [Mg/Fe] ratios. Our sample consists of 592 stars with low [Mg/Fe] from the bar; 698 stars with high [Mg/Fe] from the bar; 985 stars with low [Mg/Fe] and high-eccentricity, nonbar orbits; 1471 stars with high [Mg/Fe] and high-eccentricity, nonbar orbits; 890 stars with low [Mg/Fe] and low eccentricity; and 1136 stars with high [Mg/Fe] and low eccentricity. In Figure 4, we show the distribution of each population in the $X_{\rm Gal}$–$Y_{\rm Gal}$ and $Z_{\rm Gal}$–$R_{\rm Gal}$ planes. As expected, the bar stars with low and high [Mg/Fe] are concentrated near the Galactic center (low $R_{\rm Gal}$). The same is true for populations with high and low [Mg/Fe] and high eccentricity. However, these present a greater spread of distribution in the $X_{\rm Gal}$–$Y_{\rm Gal}$ and $Z_{\rm Gal}$–$R_{\rm Gal}$ planes, probably because they are related to the spheroidal component of the bulge. On the other hand, populations with high and low [Mg/Fe] and low eccentricity are located in the outermost regions of the bulge bar, generally showing $R_{\rm Gal} > 2$ kpc.

4. Abundance Gradients of the Bulge Bar Populations

In this section, we present and discuss the radial abundance gradients of the [X/H] and [X/Fe] ratios for odd-Z (Al and K), alpha (Mg, Si, and Ca), iron-peak (Mn, Co, Ni, and Fe), and neutron-capture (Ce and Nd) elements. We estimate gradients for each of the six main populations discussed in the previous section. For each elemental gradient, we compute the best linear fits using the maximum likelihood, with associated uncertainties estimated through the Markov Chain Monte Carlo routine from the `emcee` Python package (D. Foreman-Mackey et al. 2013), as previously done in J. Donor et al. (2020) and J. V. Sales-Silva et al. (2022) for the thin-disk gradients of open clusters. In Tables 1 and 2 in Appendix A, we show the radial gradients and intercept values estimated for different abundance ratios for the low- and high-[Mg/Fe] populations. Figures 5 and 6 present the best-fit slopes d[X/H]$/dR_{\rm Gal}$ and d[X/Fe]$/dR_{\rm Gal}$ for the elements X = Mg, Si, Ca, Al, K, Mn, Co, Ni, Ce, and Nd derived for the six populations in our sample.

To better visualize the chemical abundance gradients in the different inner Galaxy populations studied here, in Figures 7 and 8 we show the median [X/H] (dividing $R_{\rm Gal}$ into six bins) as a function of the Galactocentric distance for the elements Si, Mg, Ca, Al, K, Mn, Co, Ni, and Fe in the six inner Galaxy populations studied here: high-eccentricity, nonbar stars and stars in the bar with high and low [Mg/Fe] (Figure 7), and low-eccentricity stars with high and low [Mg/Fe] (Figure 8). In Figure 9, we present the gradients of the neutron-capture elements for all bulge bar populations. In Figures 11, 12, and 13 in Appendix B, we show similar plots, but for the [X/Fe] ratios.

4.1. Low-[Mg/Fe] Populations

The MW thin disk is a stellar population that follows the low-[α/Fe] sequence (e.g., T. Bensby et al. 2003; K. Fuhrmann 2011; F. Anders et al. 2014; M. R. Hayden et al. 2014; A. Recio-Blanco et al. 2014; A. B. A. Queiroz et al. 2020). The radial metallicity gradient of the thin disk, as measured from open clusters, traces a general decay in metallicity over the range 5 kpc $\lessapprox R_{\rm Gal} \lessapprox$ 12 kpc, reaching a plateau in the outer disk (e.g., L. Spina et al. 2022; L. Magrini et al. 2023; J. M. Otto et al. 2026), with the slope of the radial metallicity gradient varying between roughly -0.05 and -0.08 dex kpc^{-1} not counting the plateau region (Y. C. Joshi et al. 2024). The disk abundance gradients of [X/Fe] ratios for some elements, such as Al, K, Mg, Si, Ca, Mn, Co, and Ni, may not show a break in the trend (e.g., N. Myers et al. 2022; J. Carbajo-Hijarrubia et al. 2024), and, in general, the present [X/Fe] abundance gradients for thin-disk populations are approximately zero (e.g., L. Spina et al. 2021; N. Myers et al. 2022; L. Magrini et al. 2023; J. Carbajo-Hijarrubia et al. 2024), with some exceptions, such as some elements formed by neutron capture (Ba and Nd, L. Magrini et al. 2023; Ce, N. Myers et al. 2022).

For field stars, metallicity gradients estimated using red giant field stars from the thin disk are also generally within -0.02 to -0.07 dex kpc^{-1} for $|Z| < 1.75$ kpc (e.g., C. Boeche et al. 2014; F. Anders et al. 2017; A.-C. Eilers et al. 2022; F. Anders et al. 2023; J. Imig et al. 2023; E. Willett et al. 2023; J. W. Johnson et al. 2025). In particular, using a red giant and red clump sample from APOGEE, J. Imig et al. (2023) found that the metallicity gradient flattens with distance from the midplane. Using a representative sample of red giant stars from the GALAH survey, K. Wang et al. (2024) estimated a metallicity gradient of $\sim -0.029 \pm 0.003$ dex kpc^{-1} for the disk in the solar neighborhood ($R_{\rm Gal} = 7$–9 kpc), a gradient similar to that found by L. Stanghellini & M. Haywood (2018) for thin-disk planetary nebulae ($d[{\rm O/H}]/dR_{\rm Gal} = -0.021$) over a wider range of $R_{\rm Gal}$ (6–16 kpc).

In addition, chemical gradients evolve over time (e.g., F. Anders et al. 2017, 2023; I. Minchev et al. 2018; B. Ratcliffe et al. 2023; E. Willett et al. 2023). Using combined asteroseismic data of red giant stars from CoRoT and spectroscopic observations from APOGEE, F. Anders et al. (2017) found that the metallicity gradient flattens from a negative value of -0.066 dex kpc^{-1} at ages of 1–4 Gyr to -0.030 dex kpc^{-1} for stars with ages between 6 and 10 Gyr. Similar results were also found in other studies (e.g., E. Willett et al. 2023, using asteroseismic ages from K2 and APOGEE data; F. Anders et al. 2023, with APOGEE and Kepler data, and machine learning to transfer labels from the seismic ages of A. Miglio et al. 2021a). Using a red giant sample from APOGEE and estimated birth radii, B. Ratcliffe et al. (2023) found flattening and inversion of the chemical gradient of the disk in older populations due to radial migration. In the latter study, the [X/H] gradients for Al, Mg, Ca, and Mn, which are initially negative, tend to flatten over time. In the case of [X/Fe] ratios, the gradient evolves from positive to approximately zero or slightly negative values for Al, Mg, Ca, and Mn.

Given observational limitations, few studies in the literature have analyzed abundance gradients with a focus on the most central region of the the MW. J. Imig et al. (2023) found a negative metallicity gradient for low-α disk field stars located roughly between 2 and 5 kpc from the Galactic center. In addition, J. Imig et al. (2023) found a slightly positive metallicity gradient for the inner high-α disk.

In our sample, two of the low-[Mg/Fe] populations show an approximately flat metallicity gradient (close to the zero-slope dashed line in the bottom panel of Figure 5): the low-[Mg/Fe] members of the bar and the low-[Mg/Fe], high-eccentricity stars. In contrast, the low-[Mg/Fe] population of stars with low-eccentricity orbits is the only one that exhibits a slight negative gradient ($d[{\rm Fe/H}]/dR_{\rm Gal} = -0.014 \pm 0.007$). The latter stars are located at $R_{\rm Gal} > 2.0$ kpc (i.e., are not in the regions closest to the Galactic center, like the other low-[Mg/Fe] populations), and they exhibit more circular orbits when compared to those in the other two low-[Mg/Fe] populations, being the population in our sample that is more similar to the thin disk. It is important to note, however, that the [Fe/H] gradient of the low-[Mg/Fe], low-eccentricity population is significantly less steep than the gradient of the outer regions of the thin disk, indicating that there may be a break in the gradient trend of the thin disk at $R_{\rm Gal} \approx 5$–6 kpc, if we compare, for example, with the APOGEE gradients -0.06 dex/kpc of field stars with distances larger than $\sim$5 kpc (J. Imig et al. 2023). Using APOGEE DR16 red giant stars covering Galactocentric radii of $0 < R_{\rm Gal} < 20$ kpc, A.-C. Eilers et al. (2022) did not find this break in the gradient of the inner low-α disk.

For the population of low-[Mg/Fe], low-eccentricity stars, the mean [Fe/H] abundance at $R_{\rm Gal} \sim 2$ kpc is $<[{\rm Fe/H}]> \sim +0.15$ (Figure 8), which is similar to the mean metallicity of $<[{\rm Fe/H}]> \sim +0.12$ found for a sample of stars within 30 pc of the Galactic center in the early near-infrared high-resolution study of K. Cunha et al. (2007; see also more recent work of G. Nandakumar et al. 2025 and N. Ryde et al. 2025). Such results may point to the constancy of metallicity toward the center of the Galaxy for the giant stars.

In general, the [X/H] gradients of the other elements for the low-[Mg/Fe] populations follow the trend shown by [Fe/H], except for the neutron-capture elements cerium and neodymium (see Figure 5). Both Ce and Nd can be produced through either slow or rapid neutron captures (the *s*-process and the *r*-process, respectively), with Ce being mostly an *s*-process element and Nd having a more significant fraction coming from the *r*-process (N. Prantzos et al. 2020). The *s*-process synthesizes Ce and Nd mainly in low- and intermediate-mass AGB stars (M. Lugaro et al. 2003), while the *r*-process can produce these elements in neutron star–neutron star (e.g., F. K. Thielemann et al. 2017; D. Watson et al. 2019) or black hole–neutron star (e.g., N. Ekanger et al. 2023) mergers, as well as core-collapse (e.g., J. C. Wheeler et al. 1998; N. Ekanger et al. 2023) or magnetorotational (e.g., C. Winteler et al. 2012; M. Reichert et al. 2021, 2023) supernovae. As pointed out in J. V. Sales-Silva et al. (2024), the low [Ce/Nd] ratios observed in (mainly metal-poor) bulge bar stars indicate ancient enrichment dominated by the *r*-process, possibly a signature of magnetorotational supernovae yields generated through massive stars. R. Razera et al. (2022) also note that the chemical abundances of these heavy elements in the metal-poor bulge population may have a significant contribution from massive rotating stars. The Ce and Nd gradients for stars with low [Mg/Fe] and low eccentricity show positive values (mainly Ce), but these also present larger uncertainties, associated with the larger abundance errors estimated in C. R. Hayes et al. (2022).

The [X/Fe] gradients indicate the production of a given element relative to the production of iron at different $R_{\rm Gal}$, unlike the [X/H] ratios, which have a strong dependence on star formation. [X/Fe] gradient values close to zero indicate a similar trend with $R_{\rm Gal}$ between the element and iron with Galactocentric distance. Most of the [X/Fe] gradients for the different elements for low-[Mg/Fe] populations show a constant trend, with approximately zero gradient. The exceptions are Ce and Nd for the three low-[Mg/Fe] populations; Mn for the low-[Mg/Fe] bar members and for the low-[Mg/Fe], low-eccentricity population; and K for the low-[Mg/Fe], low-eccentricity population. In the thin-disk context, near-zero [X/Fe] slopes are also found for the low-α population (e.g., B. L. Ratcliffe & M. K. Ness 2023). For the [Ce/Fe] gradient, B. L. Ratcliffe & M. K. Ness (2023) found a reversal behavior depending on the bin of ([Fe/H], [Mg/Fe]). G. Casali et al. (2023) found a strong dependence of the [Ce/Fe] abundances on $R_{\rm Gal}$ and related this behavior of [Ce/Fe] to different star formation histories and the metallicity dependence of stellar yields. Corroborating this result, J. V. Sales-Silva et al. (2024) found a spatial chemical dependence of the Ce and Nd abundances in the inner Galaxy.

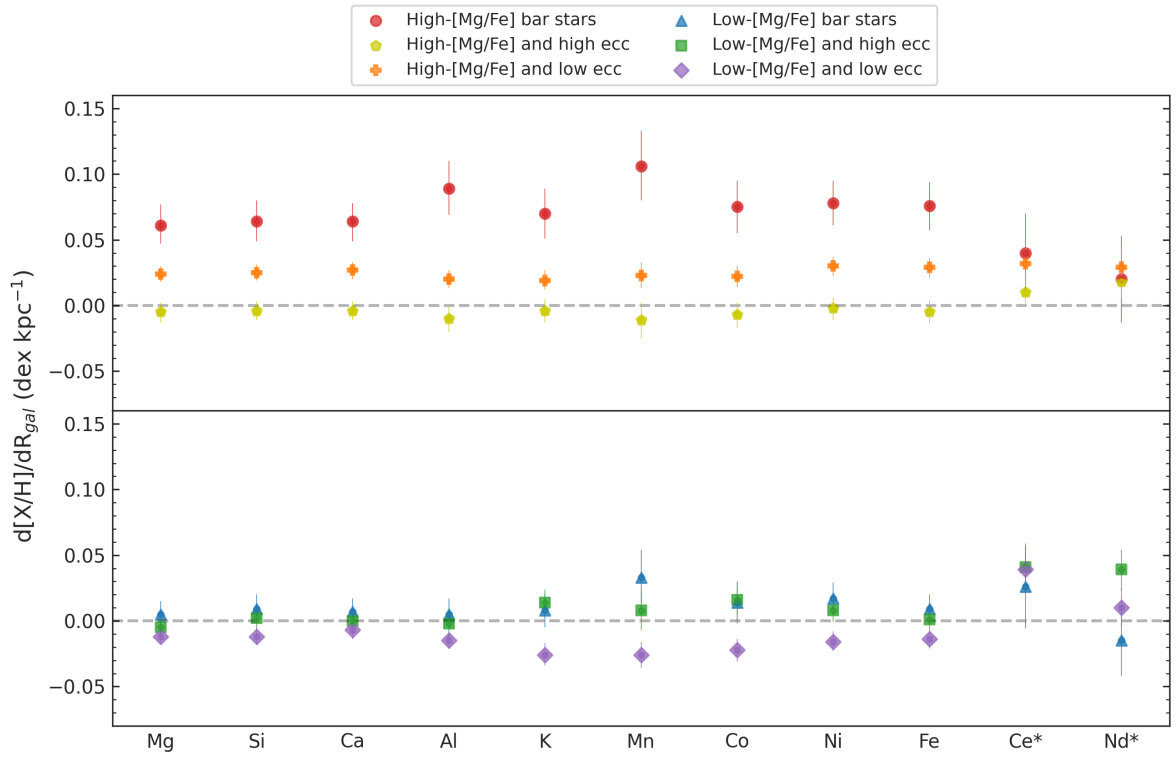

Figure 5. The gradient $d[X/H]/dR_{Gal}$ of Mg, Si, Ca, Al, K, Mn, Co, Ni, Ce, and Nd for different stellar populations. The asterisks at Ce and Nd indicate the use of the smaller sample in the gradient estimation. The legend indicates the stellar populations corresponding to each symbol. The lines in each circle represent the uncertainties of the gradients.

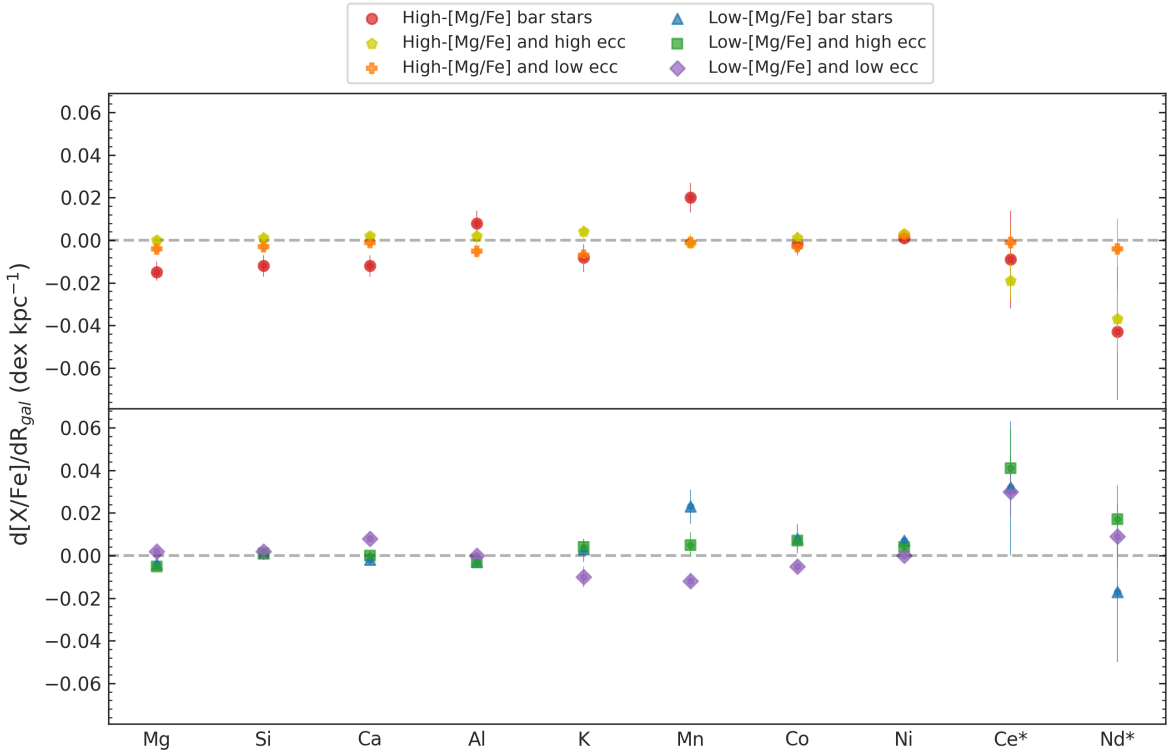

Figure 6. The gradient $d[X/Fe]/dR_{Gal}$ for Mg, Si, Ca, Al, K, Mn, Co, Ni, Ce, and Nd for different stellar populations. The asterisks at Ce and Nd indicate the use of the smaller sample in the gradient estimation. The symbols are the same as in Figure 5.

Overall, manganese is the iron-peak element that displays the largest difference between the gradients of the different low-[Mg/Fe] populations. Mn is a pristine tracer of Type Ia supernovae (K. Iwamoto et al. 1999; C. Kobayashi et al. 2006), more than iron, which exhibits significant production by core-collapse supernovae (e.g., Ó. Rodríguez et al. 2023). Among

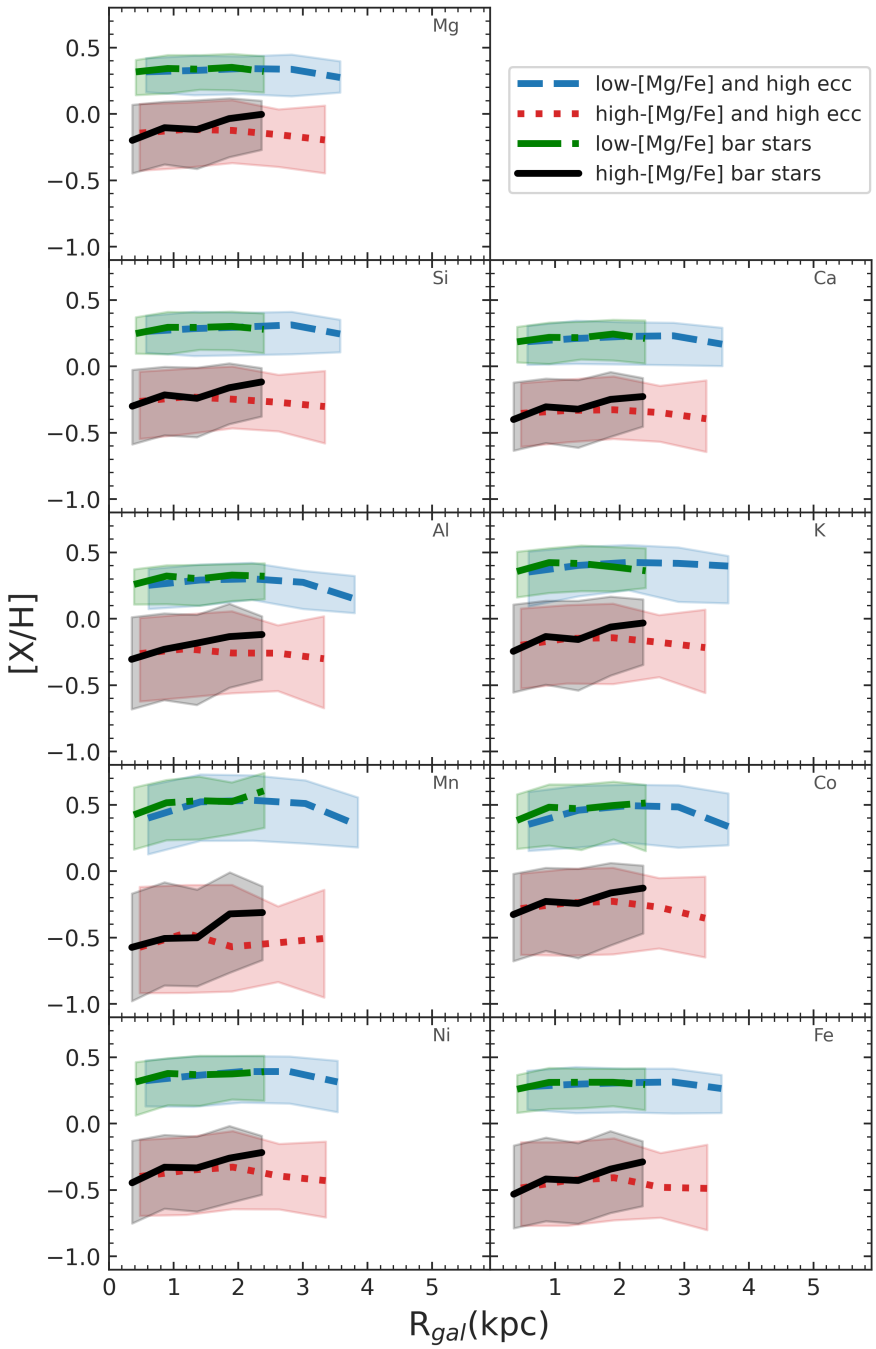

Figure 7. The [X/H] abundance ratio as a function of Galactocentric distance for the high-eccentricity, nonbar, and bar populations. The distinct lines represent the median trends of the bulge bar populations, with the shaded areas indicating the standard deviation. The legend box above the panels indicates the meaning of the different lines.

the elements in the Fe peak, the [Mn/H] gradient for the low-[Mg/Fe] and low-eccentricity population is steeper (d[Mn/H]/$dR_{\rm Gal} = -0.026^{+0.010}_{-0.010}$). On the other hand, the low [Mg/Fe] of the bar population presents a positive gradient (d[Mn/H]/$dR_{\rm Gal} = 0.033$) but with a significant uncertainty ($\approx$0.020).

The [K/H] gradient has the same negative value as the [Mn/H] gradient. Like Fe, this odd-Z element can be ejected into the ISM by Type Ia and Type II supernovae, and its production depends on several parameters, such as the metallicity of the Type Ia supernova progenitor, stellar rotation (N. Prantzos et al. 2018), and the neutrino processes in core-collapse supernovae (C. Kobayashi & N. Nakasato 2011). Potassium is also produced in super–asymptotic giant branch (P. Ventura et al. 2012) and pair-instability supernovae (E. Carretta et al. 2013).

The [X/H] gradients of the alpha elements are more similar to the Fe gradient than the Mn gradient. Alpha elements (such as Mg, Ca, and Si) are the main tracers of core-collapse supernovae (S. E. Woosley & T. A. Weaver 1995). Overall, the gradients of these elements show approximately flat values for the three low-[Mg/Fe] populations, with the low-eccentricity population showing slightly negative values.

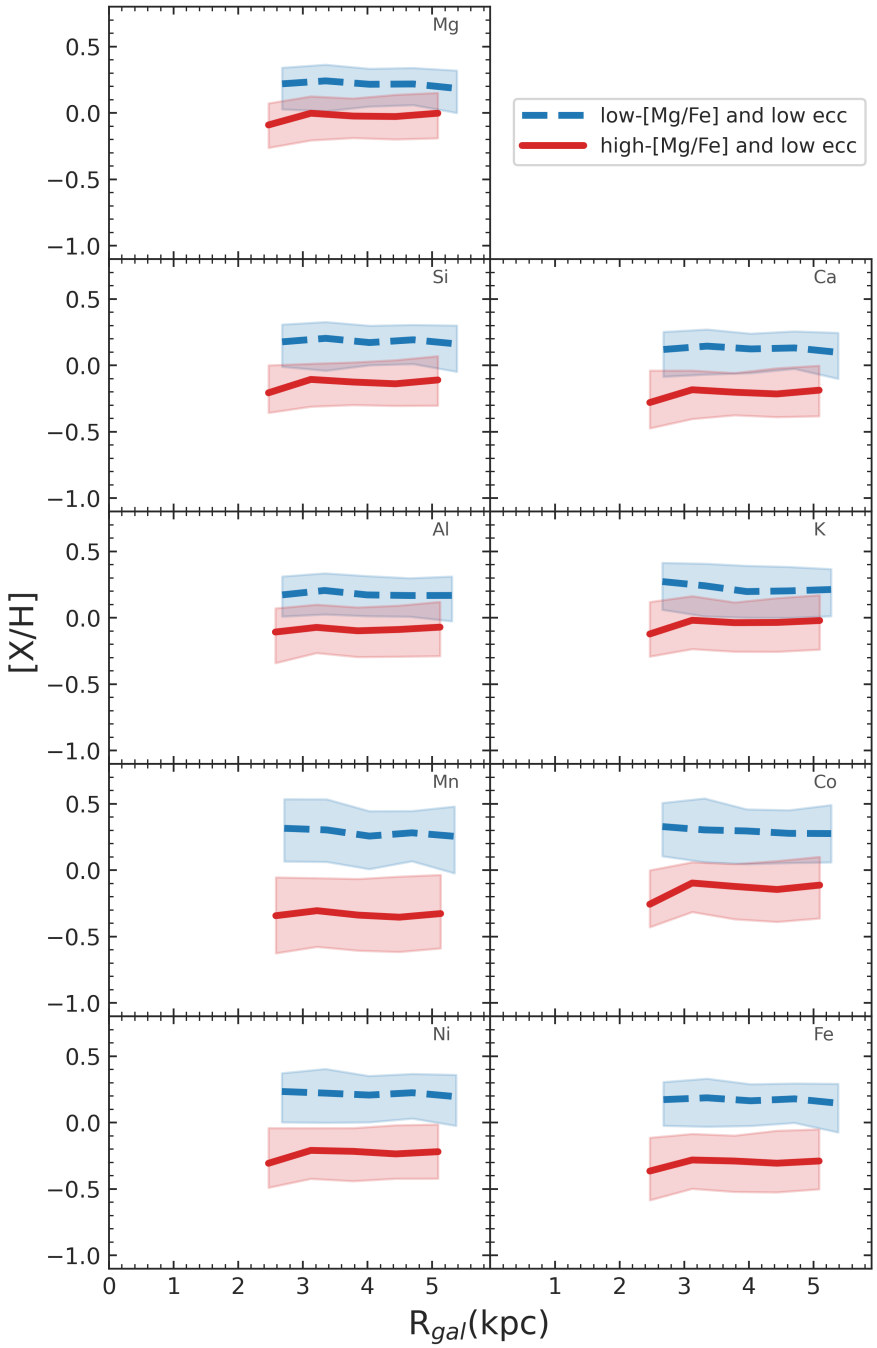

Figure 8. The [X/H] abundance ratio as a function of Galactocentric distance for low-eccentricity bulge bar populations. The distinct lines represent the median trends of the bulge bar populations, with the shaded areas indicating the standard deviation. The legend box above the panels indicates the meaning of the different lines.

4.2. High-[Mg/Fe] Populations

In the top panels of Figures 5 and 6, we show the gradients for the high-[Mg/Fe] populations, and these results can be compared to those of the low-[Mg/Fe] populations discussed in the previous subsection and shown in the bottom panels of Figures 5 and 6.

For most of the elements, the [X/H] gradients for high-[Mg/Fe], high-eccentricity stars have slopes close to zero, and this is also what we find for the gradients of the low-[Mg/Fe], high-eccentricity population. The only exceptions are the neutron-capture elements Ce and Nd, which show positive gradients. On the other hand, for bar populations and stars with low eccentricity, there is a significant difference in the [X/H] gradient between low- and high-[Mg/Fe] stars. In general, the low- and high-[Mg/Fe] populations with low eccentricity show opposite signs of the [X/H] gradient, being positive for high-[Mg/Fe] stars and negative for low-[Mg/Fe] populations. The exceptions again are the neutron-capture elements Ce and Nd, which show the same (positive) gradients between the low- and high-[Mg/Fe] stars. For example, the metallicity gradient for the high-[Mg/Fe], low-eccentricity stars is $d[\mathrm{Fe/H}]/dR_{\mathrm{Gal}} = +0.029^{+0.007}_{-0.008}$ dex kpc^{-1}, while the metallicity gradient for the low-[Mg/Fe], low-eccentricity population

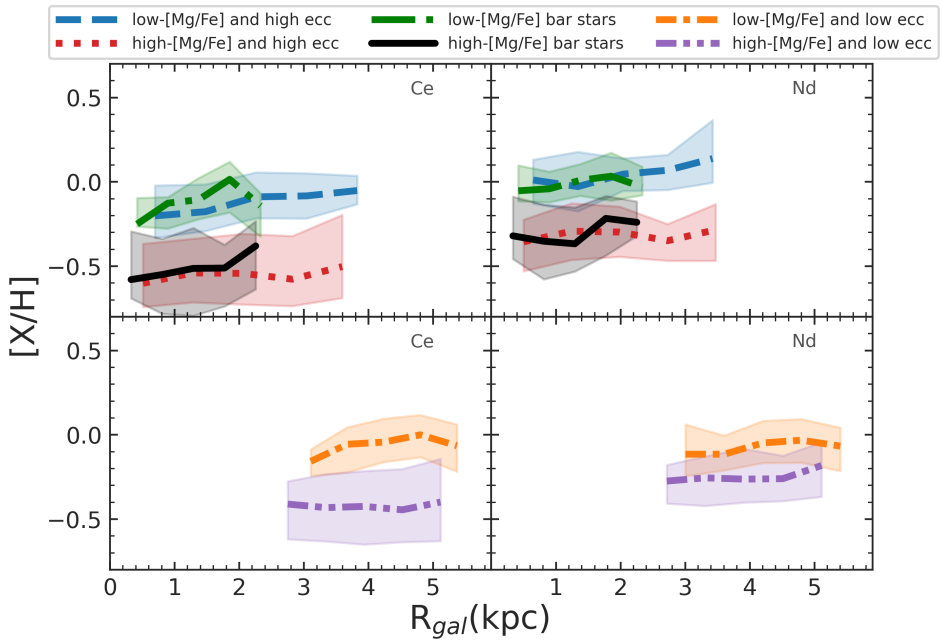

Figure 9. The [Ce/H] and [Nd/H] abundance ratios as a function of Galactocentric distance for bulge bar populations using abundances from BAWLAS catalog. The distinct lines represent the median trends, with the shaded areas indicating the standard deviation. The legend box above the panels indicates the meaning of the different lines.

is $d[\mathrm{Fe/H}]/dR_{\mathrm{Gal}} = -0.014 \pm 0.007$ dex kpc^{-1}. The high-[Mg/Fe], low-eccentricity stars present more circular orbits compared to the stars of the other high-[Mg/Fe] populations, and they are located at $R_{\mathrm{Gal}} > 2.0$ kpc. Such a population resembles both chemically (high [Mg/Fe]) and kinematically the thick-disk stars. As shown by observations (e.g., K. Carrell et al. 2012; W. Sun et al. 2024) and chemodynamical simulations for a structural thick disk (e.g., I. Minchev et al. 2014; M. S. Miranda et al. 2016; C. Li & G. Zhao 2017), the metallicity gradient of the thick disk may present positive and inverted values compared to the thin disk, a consequence of the flaring of mono-age populations, which causes a mixture of stars of different ages at a given Z, an effect known as Simpson's paradox or the Yule–Simpson effect (I. Minchev et al. 2019). In addition, the thick disk had a turbulent formation and radial migration of its old population, which influences the characterization of its chemical gradient. Thus, opposite trends in the gradients between the low- and high-[Mg/Fe] populations with low eccentricity may correspond to different epochs (or mixtures of stellar population ages) and formation processes of these populations, as for stars in thin and thick disks.

The stellar populations in our sample that present steeper positive [X/H] gradients ($d[\mathrm{X/H}]/dR_{\mathrm{Gal}} > +0.060$ dex kpc^{-1}, except for Ce and Nd) are the high-[Mg/Fe] stars of the bar. In particular, the element with the steepest gradient is [Mn/H], with a slope of $d[\mathrm{Mn/H}]/dR_{\mathrm{Gal}} = +0.106$ dex kpc^{-1}, which indicates increasing Mn abundances with increasing R_{Gal}. When ratioed to Fe, we observe that Mn is the only element that has a positive value for the [X/Fe] gradient ($d[\mathrm{Mn/Fe}]/dR_{\mathrm{Gal}} = +0.023$ dex kpc^{-1}) in the high-[Mg/Fe] stars of the bar. Within the uncertainties, the other elements have [X/Fe] gradients that are nearly zero, with only a small scatter in the mean ($d \langle\ [\mathrm{X/Fe}]\ \rangle\ /dR_{\mathrm{Gal}} = -0.007 \pm 0.010$ dex kpc^{-1}, considering all elements other than Mn, Ce, and Nd). The steep and positive [X/H] gradients found for the high-[Mg/Fe] bar population are possibly related to the formation and evolution of bar characteristics and not due to differences in the nucleosynthesis of the elements, given the zero gradients of the [X/Fe] ratios.

The presence of a bar is a relatively common feature in disk galaxies (∼50%–70% of disk galaxies in the local Universe; K. Menéndez-Delmestre et al. 2007; P. B. Nair & R. G. Abraham 2010; G. Gavazzi et al. 2015; Y. H. Lee et al. 2019), suggesting that its formation is a fundamental process in galaxy evolution. The role of different mechanisms and the precise initial conditions for bar formation remain under discussion (e.g., Y. Rosas-Guevara et al. 2025). The dominant theory for bar formation is disk instabilities (e.g., E. Athanassoula & A. Misiriotis 2002; V. P. Debattista et al. 2006). However, other processes (such as gravitational interactions) may affect the evolution of a bar. Observable properties, such as chemical gradients, help reveal the history of the bulge bar. Such steep positive gradients found for all elements in the high-[Mg/Fe] bar stars may be reminiscent of such gradients in high-redshift ($z \sim 4$–10) galaxies reported by R. Tripodi et al. (2024) based on JWST spectra. This particular redshift interval probed by R. Tripodi et al. (2024) corresponds to look-back times of about 12–13 Gyr.

Our bar sample extends to ≈2.5 kpc and includes only a few stars near the midplane ($|Z| < 0.2$ kpc; see Figure 4). Thus, it primarily traces the upper part of the peanut-shaped bulge rather than the full midplane bar, which is thought to extend to ≈4–5.5 kpc (e.g., T. Hilmi et al. 2020; J. Bland-Hawthorn & O. Gerhard 2016). In this sense, our stars occupy the same region as the red triangles in Figure 13 of F. Fragkoudi et al. (2018), which show a positive metallicity gradient along the bar's major axis up to 2.5–3 kpc, followed by an inversion beyond that radius. This pattern is also evident in our data (Figures 5 and 7).

The positive [Fe/H] gradient observed among our high-[Mg/Fe] bar stars (Figure 7) probably reflects an age variation

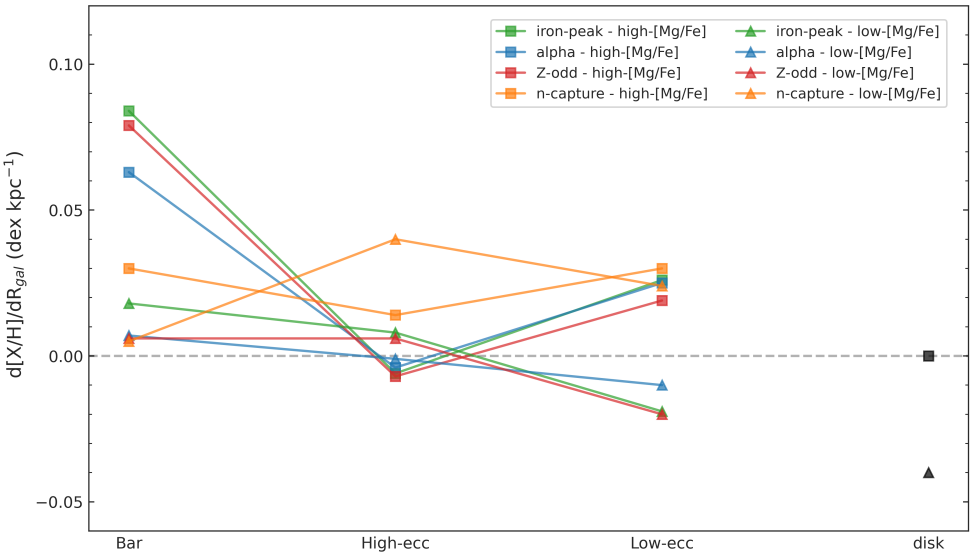

Figure 10. Average gradients of the iron-peak (Mn, Co, Ni, and Fe; green), alpha (Mg, Si, and Ca; blue), odd-Z (Al and K; red), and neutron-capture (Ce and Nd; orange) elements for six stellar populations of the inner Galaxy. Triangles and squares represent the low- and high-[Mg/Fe] populations, respectively. We connect the gradients for the same elements with a straight line. We also show the estimated metallicity gradient for the disk using giant field stars at $|Z| < 1$ kpc (J. Imig et al. 2023), using a square to represent the high-α disk and a triangle for the low-α disk.

along the peanut structure: stars closer to the Galactic center are older, while those toward the bar end are younger by a few Gyr. This interpretation agrees with the N-body simulations of P. Di Matteo et al. (2019), whose Figures 5 and 6 show that, indeed, stars at larger bar radii (and away from the midplane) are both younger and more metal-rich.

The convergence of [Fe/H] between the high- and low-[Mg/Fe] bar populations near $R_{\rm Gal} \approx 2.5$ kpc may therefore indicate that the high-[Mg/Fe] stars become progressively younger and more metal-rich with increasing radius. This inverse age–metallicity trend within the high-[Mg/Fe] sequence is also consistent with Figure 1, where [Mg/Fe], and thus stellar age, decreases by ≈0.25 dex as [Fe/H] increases from −1 to 0.

Summarizing our results, Figure 10 presents the average gradients for the iron-peak, alpha, odd-Z, and neutron-capture elements for the different populations of the inner Galaxy and for the metallicity of the low- and high-α disks of J. Imig et al. (2023) that used only abundances of APOGEE DR17 (without empirical corrections) and separated the disk populations with boundaries in the [Mg/Fe]–[Fe/H] plane similar to our limits. We observe that the estimated gradient for the Fe-peak elements for the high-[Mg/Fe], low-eccentricity stars is steeper than the estimated metallicity gradient for the high-α disk at $|Z| < 1.0$ kpc (0.000 ± 0.005 dex kpc^{-1}) (J. Imig et al. 2023). Some studies of the thick disk (e.g, F. Anders et al. 2014; M. R. Hayden et al. 2014; K. Wang et al. 2024; A. Chen et al. 2026) show similar metallicity gradient values to the gradient of the Fe-peak elements for the high-[Mg/Fe], low-eccentricity stars. Additionally, we detect a significant difference between the Fe-peak element gradients for the low-[Mg/Fe], low-eccentricity stars and the metallicity estimate for the low-α disk at $|Z| < 1.0$ kpc (-0.040 ± 0.002 dex kpc^{-1}) (J. Imig et al. 2023).

Clearly, in Figure 10, the elements produced by the neutron capture (orange symbols) generally exhibit a different behavior compared to the other elements in various populations of the inner region. This behavior for these elements is also observed on the disk (e.g, N. Myers et al. 2022; L. Magrini et al. 2023). Understanding evolution and neutron-capture element distribution is complex owing, for example, to its strong and complicated dependence on [Fe/H] and age, as shown in studies of thin-disk populations (e.g, J. V. Sales-Silva et al. 2022; G. Casali et al. 2023). Thus, beyond the significant uncertainties in the gradient estimates, the distinct gradient of Ce and Nd should be strongly associated with the age and [Fe/H] of the populations in the inner region of the Galaxy. The production efficiency of heavy s-process elements such as Ce and Nd depends strongly on metallicity, since a distinct iron content causes a change in neutrons available per seed (iron) nucleus used by the s-process, while the nature of the relationship between heavy elements and age is complex and not fully understood (e.g, M. Baratella et al. 2021). The enrichment of heavy elements in the ISM is delayed by the slow evolution of AGB stars, creating a complex link to stellar age, while uncertainties in r-process sources add further complication.

5. Conclusions

We present radial abundance gradients for ∼8000 stars from the bulge bar selected by A. B. A. Queiroz et al. (2021), using chemical abundances from APOGEE DR17 for the elements Mg, Si, Ca, Al, K, Mn, Co, Ni, and Fe. In addition, we analyzed the gradients of the heavy elements Ce and Nd using abundances from the DR17 BAWLAS catalog (C. R. Hayes et al. 2022) for a subsample of approximately 2000 bulge bar stars. This study includes analyses of α, odd-Z, iron-peak, and neutron-capture elements, providing a chemically broad view of the chemical abundance gradients in the inner MW.

The bulge bar is known to be composed of a complex mixture of multiple populations. Following J. V. Sales-Silva et al. (2024), we removed from our bulge bar sample 37 chemically peculiar stars (mostly N-rich), 37 probable GC members, and 33 possibly ex situ stars from the Heracles substructure. We segregated our sample into low- and high-[Mg/Fe] stars using the [Mg/Fe]–[Fe/H] plane and found two

chemical populations within the low-[Mg/Fe] population: one Al-poor and one K-rich. In addition, there was a small group of Ni-poor stars. These Al-poor, K-rich, and Ni-poor stars were removed from the low-[Mg/Fe] population sample.

To perform a detailed analysis of the chemical radial gradients of the different kinematical populations in the bulge bar sample, we further segregated low- and high-[Mg/Fe] populations using the $|Z_{max}|$–ecc orbital plane into six main populations: two with bar-driven orbits, two with eccentric orbits, and two with low-eccentricity orbits, with each pair being composed of stars with low and high [Mg/Fe].

Our results can be summarized as follows:

1. The low-[Mg/Fe] stars with low-eccentricity orbits located at radii 2.0 kpc $< R_{\rm Gal} <$ 6.0 kpc show a slightly negative value of the metallicity gradient (d[Fe/H]/$dR_{\rm Gal} = -0.014 \pm 0.007$ dex kpc^{-1}). This population presents orbital and chemical characteristics similar to those of thin-disk stars. However, thin-disk stars at Galactocentric distances larger than ∼5.0–6.0 kpc show a much steeper metallicity gradient of −0.06 dex kpc^{-1} (J. Imig et al. 2023). The change in slope at ∼5–6 kpc may point to a break in the global [Fe/H] gradient trend of the thin disk as it transitions to flatter gradients in the inner regions of the Galaxy.
2. The other two low-[Mg/Fe] populations in our sample show approximately flat profiles for the metallicity gradients. For the low-[Mg/Fe], high-eccentricity population, d[Fe/H]/$dR_{\rm Gal} = 0.001^{+0.09}_{-0.008}$ dex kpc^{-1}, while for the low-[Mg/Fe] bar members, d[Fe/H]/$dR_{\rm Gal} = +0.009^{+0.011}_{-0.011}$ dex kpc^{-1}.
3. In general, the [X/H] gradients of the other elements in the low-[Mg/Fe] populations follow similar trends to those followed by Fe, with the exception of those elements produced by neutron captures, Ce and Nd. The Ce and Nd gradients for stars with low [Mg/Fe] and low eccentricity show positive slopes, mainly for Ce, although the latter have larger uncertainties. Ce and Nd present a strong dependence of their production on age and [Fe/H], which probably accounts for the distinct gradient of Ce and Nd compared to other elements.
4. The [X/Fe] gradients for all elements of the three low-[Mg/Fe] populations are approximately zero, indicating similar trends between those elements and iron with Galactocentric distance. The exceptions are Ce for the three low-[Mg/Fe] populations ($d \langle$ [Ce/Fe] $\rangle$ /$dR_{\rm Gal} = +0.034 \pm 0.006$ dex kpc^{-1}), Mn for the low-[Mg/Fe] population from the bar (d[Mn/Fe]/$dR_{\rm Gal} = 0.023^{+0.008}_{-0.008}$ dex kpc^{-1}) and the low-[Mg/Fe] population with low eccentricity (d[Mn/Fe]/$dR_{\rm Gal} = -0.012^{+0.003}_{-0.004}$ dex kpc^{-1}), and K for the low-[Mg/Fe] and low-eccentricity population (d[K/Fe]/$dR_{\rm Gal} = -0.010^{+0.005}_{-0.005}$ dex kpc^{-1}). (All of these slopes are shown in Table 1.)
5. In general, the [X/H] gradients for both the low- and high-[Mg/Fe] populations having orbits with high eccentricity present approximately constant, near-zero slopes. In contrast, the low- and high-[Mg/Fe] populations having low-eccentricity orbits have [X/H] gradients with slopes of opposite signs, being positive for high-[Mg/Fe] stars and negative for low-[Mg/Fe] populations. In terms of Galactocentric distance, the high-[Mg/Fe], low-eccentricity population located at 2.0 kpc $< R_{\rm Gal} <$ 6.0 kpc chemically and kinematically resembles the thick-disk stars. This similarity also extends to the [Fe/H] gradient, since the thick disk can show positive gradient values (e.g., K. Carrell et al. 2012; W. Sun et al. 2024).
6. We found that the two bar populations (low and high [Mg/Fe]) exhibit distinct radial gradients, with the high-[Mg/Fe] population showing a positive gradient much steeper than that for the low-[Mg/Fe] bar stars, which are overall flat. This difference in the radial gradients for the bar populations may be linked to the formation of the low- and high-[Mg/Fe] components at different times and via distinct Galactic evolutionary scenarios, as occurred in the formation of the thin and thick disks. The bulge formation simulations (e.g., V. P. Debattista et al. 2017) and the chemical similarity of the thin-disk stars to the low-[Mg/Fe] bar stars are in line with the formation of this bar population through secular evolution from an early low-[Mg/Fe] thin disk. Recently, through dynamical and chemical analysis, A. Pandey & O. Gerhard (2025) obtained results indicating that the high-[Mg/Fe] bar stars originated via secular evolution from a high-α disk. The approximately constant value of the [X/Fe] gradients for high-[Mg/Fe] bar stars indicates that the steep value of the [X/H] gradient is possibly not due to issues of nucleosynthesis of the elements. We found a convergence of [Fe/H] between the high- and low-[Mg/Fe] bar populations near $R_{\rm Gal} \approx 2.5$ kpc, indicating that the high-[Mg/Fe] stars become progressively younger and more metal-rich with increasing radius.
7. We also found that the gradients for the high-[Mg/Fe] bar stars are significantly different from those of the other high-[Mg/Fe] bulge populations, with the bar population showing more positive and steep values for all elements. Our bar sample extends to ≈2.5 kpc and includes only a few stars near the midplane ($|Z| <$ 0.2 kpc). Hence, the steep positive [X/H] gradients observed among our high-[Mg/Fe] bar stars may also reflect an age variation along the upper part of the peanut-shaped bulge: stars closer to the Galactic center are older, while those toward the bar end are younger by a few Gyr. This interpretation agrees with the N-body simulations. If the high-[Mg/Fe] bar population represents the oldest stars, these results may also be related to the steep positive metallicity gradients derived by R. Tripodi et al. (2024) for high-redshift, $z \sim$ 4–10 galaxies observed with JWST. Unfortunately, bulge bar stars suffer from inaccurate age estimates, making a detailed analysis of the temporal evolution of radial gradients challenging at this point. The lack of accurate ages is a limiting factor in archaeological studies of the inner Galactic region. Future space missions providing high-precision asteroseismology in dense fields of the inner Galaxy (A. Miglio et al. 2021b) or a more robust method for estimating age through machine learning may contribute to a better understanding of the inner MW gradients.

Our results provide important observational constraints for Galactic models, particularly for bulge bar evolution, contributing to the determination of the influence of processes such as interactions with dark matter halos and gas physics related to star formation and stellar feedback.

Acknowledgments

J.V.S.-S. acknowledges the PCI program under grant 313980/2025-0 and 300523/2026-2. S.D. acknowledges CNPq/MCTI for grant 306859/2022-0 and FAPERJ for grant 210.688/2024. D.S. thanks the National Council for Scientific and Technological Development—CNPq. V.L.-T. acknowledges support from the CNPq through the Postdoctoral Junior (PDJ) fellowship, process No. 152242/2024-4. T.M. acknowledges support from MCIN for the project *PLAtoSOnG* from its grant PID2023-146453NB-100, PI: Beck). P.M.F. acknowledges support for this research from the National Science Foundation (AST-2206541). I.M. acknowledges support by the Deutsche Forschungsgemeinschaft under grant MI 2009/2-1. J.G.F.-T. gratefully acknowledges the support provided by ANID Fondecyt Regular No. 1260371, ANID Fondecyt Postdoc No. 3230001 (Sponsoring researcher), the Joint Committee ESO-Government of Chile under the agreement 2023 ORP 062/2023, and the Doctoral Program in Artificial Intelligence, DISC-UCN. M.Z. acknowledges funding from ANID BASAL Center for Astrophysics and Associated Technologies (CATA) FB210003 and from FONDECYT Regular grant No. 1230731. Funding for the Sloan Digital Sky Survey IV has been provided by the Alfred P. Sloan Foundation, the US Department of Energy Office of Science, and the Participating Institutions. SDSS-IV acknowledges support and resources from the Center for High-Performance Computing at the University of Utah. The SDSS website is www.sdss.org.

SDSS-IV is managed by the Astrophysical Research consortium for the Participating Institutions of the SDSS Collaboration, including the Brazilian Participation Group, the Carnegie Institution for Science, Carnegie Mellon University, the Chilean Participation Group, the French Participation Group, Harvard-Smithsonian Center for Astrophysics, Instituto de Astrofísica de Canarias, Johns Hopkins University, Kavli Institute for the Physics and Mathematics of the Universe (IPMU)/University of Tokyo, Lawrence Berkeley National Laboratory, Leibniz Institut fur Astrophysik Potsdam (AIP), Max-Planck-Institut fur Astronomie (MPIA Heidelberg), Max-Planck Institut fur Astrophysik (MPA Garching), Max-Planck-Institut fur Extraterrestrische Physik (MPE), National Astronomical Observatory of China, New Mexico State University, New York University, University of Notre Dame, Observatório Nacional/MCTI, The Ohio State University, Pennsylvania State University, Shanghai Astronomical Observatory, United Kingdom Participation Group, Universidad Nacional Autónoma de México, University of Arizona, University of Colorado Boulder, University of Oxford, University of Portsmouth, University of Utah, University of Virginia, University of Washington, University of Wisconsin, Vanderbilt University, and Yale University.

Facility: Sloan (APOGEE).

Software: matplotlib (J. D. Hunter 2007), Numpy (C. R. Harris et al. 2020), Scipy (P. Virtanen et al. 2020).

Appendix A
Radial Abundance Gradients and Intercept Values

In Tables 1 and 2, we present the radial gradients (m_{50}) and intercept (b_{50}) values estimated for different abundance ratios for the low- and high-[Mg/Fe] populations.

Table 1
Radial Abundance Gradients (dex kpc^{-1}) and Intercept Value of the Best Linear Fits for Different Stellar Populations in the Inner Galaxy with low [Mg/Fe] Ratio and $R_{\rm Gal} < 6$ kpc

[X/H]	m_{50}	m_{16}	m_{84}	b_{50}	b_{16}	b_{84}	[X/Fe]	m_{50}	m_{16}	m_{84}	b_{50}	b_{16}	b_{84}
Bar Stars													
Mg	0.005	−0.005	0.015	0.298	0.284	0.312	Mg	−0.004	−0.006	−0.002	0.048	0.045	0.051
Si	0.009	−0.001	0.020	0.243	0.228	0.258	Si	0.001	−0.002	0.003	−0.008	−0.011	−0.005
Ca	0.007	−0.003	0.017	0.175	0.160	0.190	Ca	−0.002	−0.004	0.001	−0.076	−0.080	−0.072
Al	0.005	−0.007	0.017	0.260	0.243	0.277	Al	−0.003	−0.006	−0.000	−0.003	−0.008	0.001
K	0.008	−0.005	0.021	0.353	0.335	0.372	K	0.003	−0.003	0.008	0.091	0.083	0.098
Mn	0.033	0.013	0.054	0.425	0.395	0.454	Mn	0.023	0.015	0.031	0.157	0.145	0.169
Co	0.014	−0.002	0.030	0.404	0.381	0.427	Co	0.008	0.001	0.015	0.140	0.130	0.150
Ni	0.017	0.005	0.029	0.306	0.289	0.323	Ni	0.007	0.004	0.009	0.049	0.046	0.053
Fe	0.009	−0.002	0.020	0.250	0.234	0.265	Fe	…	…	…	…	…	…
Ce*	0.026	−0.006	0.057	−0.170	−0.218	−0.121	Ce*	0.032	0.000	0.063	−0.387	−0.435	−0.338
Nd*	−0.015	−0.042	0.012	0.020	−0.019	0.061	Nd*	−0.017	−0.050	0.016	−0.187	−0.236	−0.138
Low-eccentricity Stars													
Mg	−0.012	−0.018	−0.005	0.244	0.217	0.271	Mg	0.002	0.001	0.004	0.044	0.038	0.050
Si	−0.012	−0.018	−0.005	0.206	0.177	0.235	Si	0.002	0.001	0.003	0.004	−0.001	0.010
Ca	−0.007	−0.014	−0.001	0.131	0.102	0.159	Ca	0.008	0.007	0.010	−0.079	−0.086	−0.073
Al	−0.015	−0.021	−0.008	0.220	0.191	0.250	Al	−0.000	−0.002	0.002	0.008	−0.001	0.017
K	−0.026	−0.034	−0.017	0.305	0.268	0.342	K	−0.010	−0.015	−0.005	0.090	0.068	0.112
Mn	−0.026	−0.036	−0.016	0.368	0.324	0.412	Mn	−0.012	−0.015	−0.008	0.158	0.142	0.174
Co	−0.022	−0.031	−0.014	0.365	0.327	0.405	Co	−0.005	−0.008	−0.002	0.145	0.131	0.159
Ni	−0.016	−0.023	−0.008	0.260	0.227	0.293	Ni	−0.000	−0.002	0.001	0.050	0.044	0.056
Fe	−0.014	−0.021	−0.007	0.200	0.170	0.230	Fe	…	…	…	…	…	…
Ce*	0.039	0.025	0.052	−0.223	−0.285	−0.162	Ce*	0.030	0.019	0.042	−0.285	−0.338	−0.236
Nd*	0.010	−0.004	0.025	−0.103	−0.166	−0.038	Nd*	0.009	−0.006	0.024	−0.188	−0.256	−0.120
High-eccentricity Stars													
Mg	−0.005	−0.012	0.002	0.283	0.269	0.297	Mg	−0.005	−0.007	−0.004	0.051	0.048	0.054
Si	0.002	−0.006	0.009	0.226	0.212	0.240	Si	0.001	0.000	0.003	−0.007	−0.009	−0.004
Ca	0.000	−0.007	0.008	0.158	0.144	0.172	Ca	0.000	−0.001	0.002	−0.077	−0.080	−0.074
Al	−0.002	−0.012	0.009	0.226	0.205	0.246	Al	−0.003	−0.005	−0.002	−0.008	−0.012	−0.004
K	0.014	0.005	0.024	0.312	0.293	0.330	K	0.004	0.001	0.007	0.091	0.085	0.098
Mn	0.008	−0.007	0.023	0.410	0.380	0.442	Mn	0.005	−0.000	0.011	0.173	0.162	0.184
Co	0.016	0.005	0.027	0.363	0.342	0.384	Co	0.007	0.003	0.010	0.139	0.132	0.145
Ni	0.008	−0.001	0.016	0.292	0.275	0.309	Ni	0.004	0.002	0.005	0.054	0.052	0.057
Fe	0.001	−0.007	0.009	0.231	0.215	0.246	Fe	…	…	…	…	…	…
Ce*	0.041	0.023	0.059	−0.220	−0.260	−0.180	Ce*	0.041	0.024	0.059	−0.386	−0.424	−0.348
Nd*	0.039	0.023	0.054	−0.040	−0.071	−0.008	Nd*	0.017	−0.000	0.033	−0.219	−0.254	−0.184

Note. Also given are the 16th and 84th percentiles of the abundance gradients and of the intercept.

Table 2
Radial Abundance Gradients (dex kpc^{-1}) and Intercept Values of the Best Linear Fits for Different Stellar Populations in the Inner Galaxy with High [Mg/Fe] Ratio and $R_{Gal} < 6$ kpc

[X/H]	m_{50}	m_{16}	m_{84}	b_{50}	b_{16}	b_{84}	[X/Fe]	m_{50}	m_{16}	m_{84}	b_{50}	b_{16}	b_{84}
Bar Stars													
Mg	0.061	0.047	0.077	−0.208	−0.228	−0.189	Mg	−0.015	−0.019	−0.010	0.300	0.295	0.306
Si	0.064	0.049	0.080	−0.318	−0.337	−0.299	Si	−0.012	−0.017	−0.007	0.190	0.184	0.197
Ca	0.064	0.049	0.078	−0.400	−0.419	−0.381	Ca	−0.012	−0.017	−0.007	0.107	0.101	0.114
Al	0.089	0.069	0.110	−0.370	−0.397	−0.344	Al	0.008	0.002	0.014	0.147	0.139	0.154
K	0.070	0.051	0.089	−0.250	−0.275	−0.226	K	−0.008	−0.015	−0.002	0.263	0.255	0.271
Mn	0.106	0.080	0.133	−0.614	−0.650	−0.578	Mn	0.020	0.013	0.027	−0.073	−0.083	−0.064
Co	0.075	0.055	0.095	−0.360	−0.386	−0.335	Co	−0.002	−0.007	0.004	0.154	0.147	0.161
Ni	0.078	0.061	0.095	−0.447	−0.469	−0.424	Ni	0.001	−0.002	0.003	0.064	0.060	0.067
Fe	0.076	0.057	0.094	−0.510	−0.533	−0.486	Fe	…	…	…	…	…	…
Ce*	0.040	0.010	0.070	−0.560	−0.597	−0.524	Ce*	−0.009	−0.032	0.014	−0.013	−0.041	0.016
Nd*	0.020	−0.013	0.053	−0.332	−0.373	−0.292	Nd*	−0.043	−0.075	−0.012	0.161	0.123	0.199
Low-Eccentricity Stars													
Mg	0.024	0.018	0.030	−0.136	−0.160	−0.1116	Mg	−0.004	−0.007	−0.002	0.280	0.270	0.289
Si	0.025	0.019	0.031	−0.242	−0.267	−0.217	Si	−0.003	−0.005	−0.000	0.172	0.163	0.182
Ca	0.027	0.020	0.033	−0.322	−0.348	−0.296	Ca	−0.001	−0.003	0.001	0.090	0.081	0.099
Al	0.020	0.013	0.027	−0.187	−0.218	−0.158	Al	−0.005	−0.008	−0.003	0.214	0.202	0.226
K	0.019	0.012	0.027	−0.131	−0.161	−0.100	K	−0.007	−0.011	−0.003	0.273	0.257	0.289
Mn	0.023	0.013	0.033	−0.434	−0.476	−0.392	Mn	−0.001	−0.003	0.002	−0.036	−0.047	−0.026
Co	0.022	0.014	0.030	−0.237	−0.270	−0.203	Co	−0.003	−0.006	−0.000	0.171	0.160	0.182
Ni	0.030	0.022	0.037	−0.354	−0.383	−0.324	Ni	0.002	0.001	0.003	0.057	0.052	0.062
Fe	0.029	0.021	0.036	−0.417	−0.449	−0.386	Fe	…	…	…	…	…	…
Ce*	0.032	0.020	0.044	−0.550	−0.602	−0.498	Ce*	−0.001	−0.008	0.006	−0.078	−0.108	−0.049
Nd*	0.029	0.017	0.041	−0.364	−0.415	−0.313	Nd*	−0.004	−0.017	0.010	0.024	−0.032	0.079
High-Eccentricity Stars													
Mg	−0.005	−0.013	0.002	−0.154	−0.166	−0.142	Mg	−0.000	−0.002	0.002	0.294	0.291	0.298
Si	−0.004	−0.011	0.003	−0.264	−0.275	−0.252	Si	0.001	−0.001	0.004	0.184	0.180	0.188
Ca	−0.004	−0.011	0.003	−0.344	−0.355	−0.332	Ca	0.002	−0.001	0.004	0.102	0.098	0.106
Al	−0.010	−0.020	0.000	−0.272	−0.289	−0.256	Al	0.002	−0.002	0.005	0.165	0.160	0.171
K	−0.004	−0.013	0.005	−0.192	−0.208	−0.178	K	0.004	0.000	0.007	0.248	0.242	0.254
Mn	−0.011	−0.025	0.002	−0.504	−0.526	−0.481	Mn	−0.001	−0.004	0.003	−0.059	−0.065	−0.053
Co	−0.007	−0.017	0.002	−0.290	−0.306	−0.274	Co	0.001	−0.002	0.004	0.157	0.152	0.161
Ni	−0.002	−0.011	0.006	−0.384	−0.398	−0.370	Ni	0.003	0.001	0.004	0.065	0.063	0.067
Fe	−0.005	−0.014	0.004	−0.449	−0.463	−0.434	Fe	…	…	…	…	…	…
Ce*	0.010	−0.001	0.022	−0.563	−0.584	−0.543	Ce*	−0.019	−0.028	−0.009	0.022	0.006	0.037
Nd*	0.018	0.006	0.031	−0.352	−0.372	−0.332	Nd*	−0.037	−0.052	−0.023	0.179	0.155	0.203

Note. We also show the 16th and 84th percentiles of the abundance gradients and of the intercept.

Appendix B
[X/Fe] Radial Gradients of the Studied Bulge Bar Populations

In Figures 11 and 12, we show the median [X/Fe] (dividing $R_{\rm Gal}$ into six bins) as a function of the Galactocentric distance for the elements Si, Mg, Ca, Al, K, Mn, Co, Ni, and Fe. In Figure 13, we show similar plots, but for Ce and Nd elements.

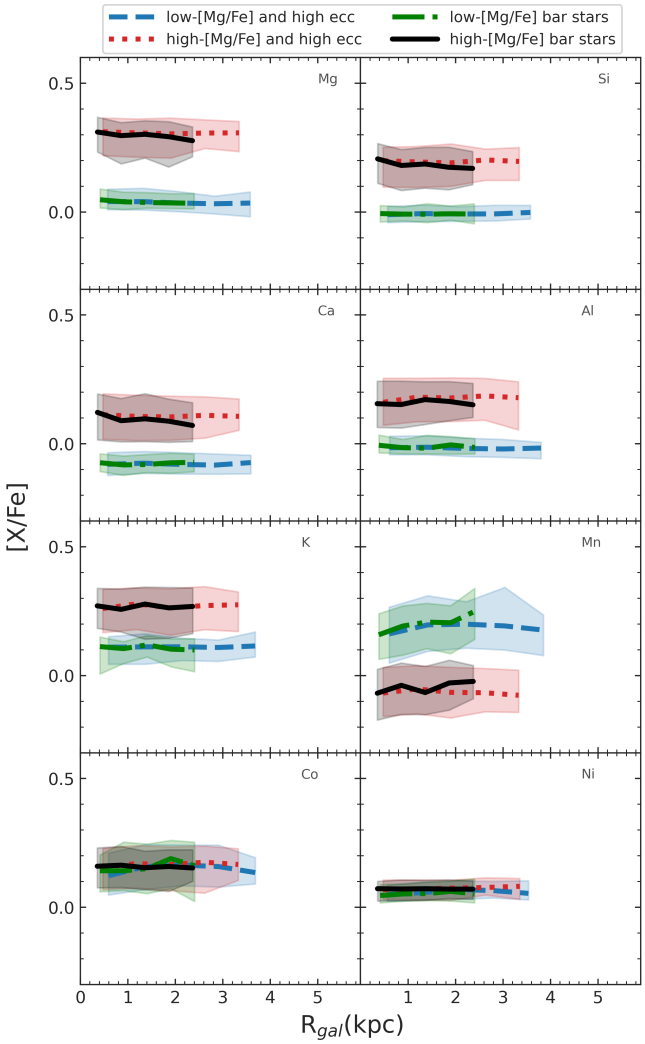

Figure 11. The [X/Fe] abundance ratio as a function of Galactocentric distance for the high-eccentricity and bar populations. The distinct lines represent the median trends of the bulge bar populations, with the shaded areas indicating the standard deviation. The legend above the panels describes the meaning of the different lines.

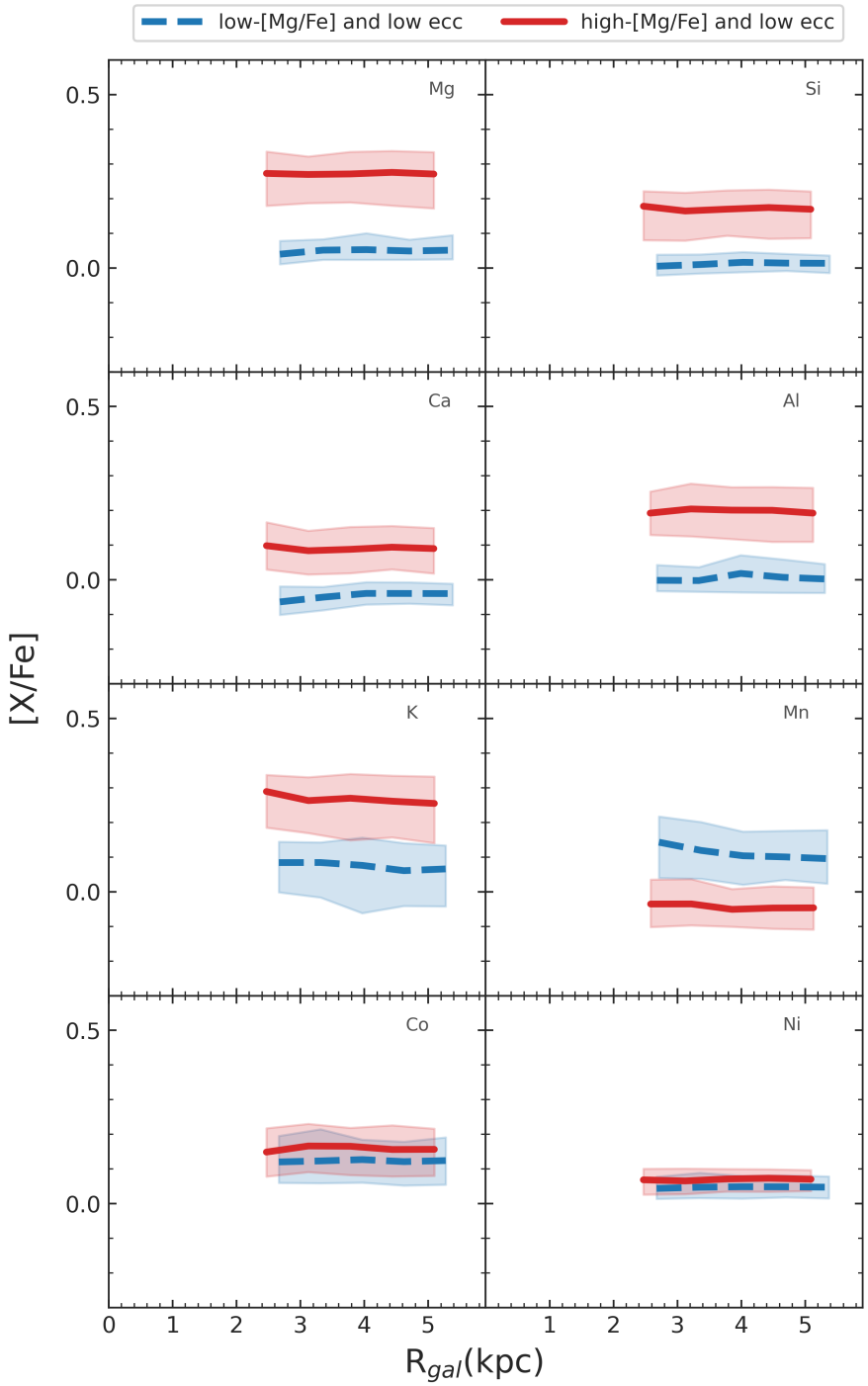

Figure 12. The [X/Fe] abundance ratio as a function of Galactocentric distance for low-eccentricity bulge bar populations. The distinct lines represent the median trends of the bulge bar populations, with the shaded areas indicating the standard deviation. The legend above the panels indicates the meaning of the different lines.

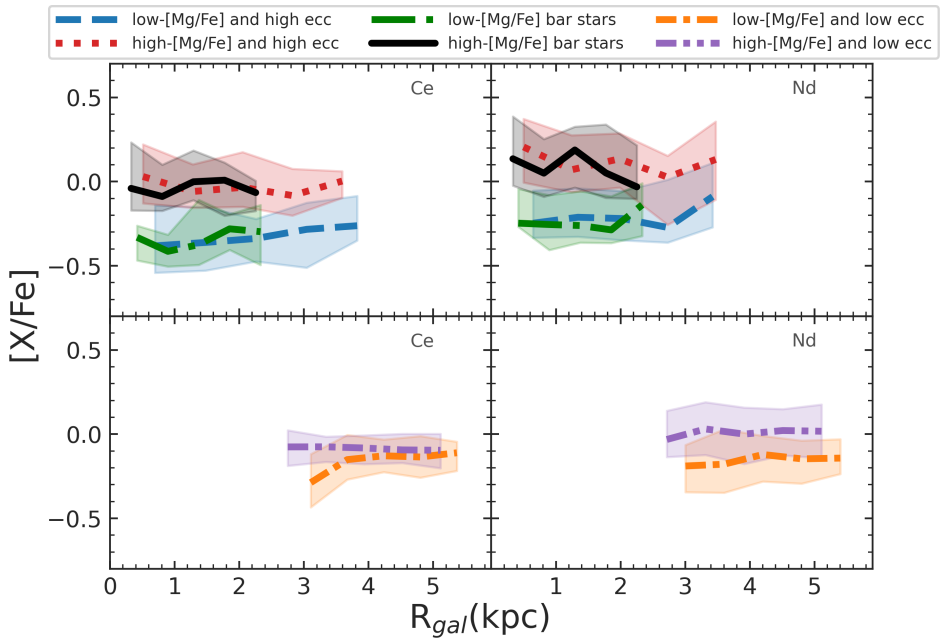

Figure 13. The [Ce/Fe] and [Nd/Fe] abundance ratios as a function of Galactocentric distance for bulge bar populations using abundances from the BAWLAS catalog. The distinct lines represent the median trends, with the shaded areas indicating the standard deviation. The legend above the panels describes the meaning of the different lines.

ORCID iDs

J. V. Sales-Silva https://orcid.org/0000-0003-0636-7463
K. Cunha https://orcid.org/0000-0001-6476-0576
V. V. Smith https://orcid.org/0000-0002-0134-2024
S. Daflon https://orcid.org/0000-0001-9205-2307
D. Souto https://orcid.org/0000-0002-7883-5425
R. Guerço https://orcid.org/0000-0002-0151-5212
V. Loaiza-Tacuri https://orcid.org/0000-0003-0506-8269
I. Minchev https://orcid.org/0000-0002-5627-0355
S. R. Majewski https://orcid.org/0000-0003-2025-3147
B. Barbuy https://orcid.org/0000-0001-9264-4417
D. Bizyaev https://orcid.org/0000-0002-3601-133X
José G. Fernández-Trincado https://orcid.org/0000-0003-3526-5052
Peter M. Frinchaboy https://orcid.org/0000-0002-0740-8346
Henrik Jönsson https://orcid.org/0000-0002-4912-8609
N. Prantzos https://orcid.org/0000-0002-4591-6253
R. P. Schiavon https://orcid.org/0000-0002-2244-0897
M. Schultheis https://orcid.org/0000-0002-6590-1657

References

Abdurro'uf, Accetta, K., Aerts, C., et al. 2022, ApJS, 259, 35
Alvarez Garay, D. A., Mucciarelli, A., Lardo, C., Bellazzini, M., & Merle, T. 2022, ApJL, 928, L11
Anders, F., Chiappini, C., Minchev, I., et al. 2017, A&A, 600, A70
Anders, F., Chiappini, C., Santiago, B. X., et al. 2014, A&A, 564, A115
Anders, F., Gispert, P., Ratcliffe, B., et al. 2023, A&A, 678, A158
Ardern-Arentsen, A., Monari, G., Queiroz, A. B. A., et al. 2024, MNRAS, 530, 3391
Athanassoula, E., & Misiriotis, A. 2002, MNRAS, 330, 35
Baratella, M., D'Orazi, V., Sheminova, V., et al. 2021, A&A, 653, A67
Barbuy, B., Chiappini, C., & Gerhard, O. 2018, ARA&A, 56, 223
Bensby, T., Feltzing, S., Gould, A., et al. 2017, A&A, 605, A89
Bensby, T., Feltzing, S., & Lundström, I. 2003, A&A, 410, 527
Bland-Hawthorn, J., & Gerhard, O. 2016, ARA&A, 54, 529
Boeche, C., Chiappini, C., Minchev, I., et al. 2013, A&A, 553, A19
Boeche, C., Siebert, A., Piffl, T., et al. 2014, A&A, 568, A71
Bowen, I. S., & Vaughan, A. H. J. 1973, ApOpt, 12, 1430
Bragança, G. A., Daflon, S., Lanz, T., et al. 2019, A&A, 625, A120
Carbajo-Hijarrubia, J., Casamiquela, L., Carrera, R., et al. 2024, A&A, 687, A239
Carrell, K., Chen, Y., & Zhao, G. 2012, AJ, 144, 185
Carretta, E., Gratton, R. G., Bragaglia, A., et al. 2013, ApJ, 769, 40
Casali, G., Grisoni, V., Miglio, A., et al. 2023, A&A, 677, A60
Chen, A., Shen, J., Wang, C., & Huang, Y. 2026, MNRAS, 546, stag035
Cheng, J. Y., Rockosi, C. M., Morrison, H. L., et al. 2012, ApJ, 746, 149
Chiappini, C., Matteucci, F., & Romano, D. 2001, ApJ, 554, 1044
Chiu, L. T. G. 1980, ApJS, 44, 31
Cunha, K., Sellgren, K., Smith, V. V., et al. 2007, ApJ, 669, 1011
Cunha, K., & Smith, V. V. 2006, ApJ, 651, 491
Cunha, K., Smith, V. V., Hasselquist, S., et al. 2017, ApJ, 844, 145
da Silva, R., D'Orazi, V., Palla, M., et al. 2023, A&A, 678, A195
Daflon, S., & Cunha, K. 2004, ApJ, 617, 1115
Debattista, V. P., Mayer, L., Carollo, C. M., et al. 2006, ApJ, 645, 209
Debattista, V. P., Ness, M., Gonzalez, O. A., et al. 2017, MNRAS, 469, 1587
Di Matteo, P., Fragkoudi, F., Khoperskov, S., et al. 2019, A&A, 628, A11
Donor, J., Frinchaboy, P. M., Cunha, K., et al. 2020, AJ, 159, 199
Eggen, O. J., Lynden-Bell, D., & Sandage, A. R. 1962, ApJ, 136, 748
Eilers, A.-C., Hogg, D. W., Rix, H.-W., et al. 2022, ApJ, 928, 23
Ekanger, N., Bhattacharya, M., & Horiuchi, S. 2023, MNRAS, 525, 2040
Faherty, J. K., Burgasser, A. J., Cruz, K. L., et al. 2009, AJ, 137, 1
Fernández-Trincado, J. G., Beers, T. C., Barbuy, B., et al. 2022, A&A, 663, A126
Fernández-Trincado, J. G., Zamora, O., Souto, D., et al. 2019, A&A, 627, A178
Feuillet, D. K., Feltzing, S., Sahlholdt, C., & Bensby, T. 2022, ApJ, 934, 21
Foreman-Mackey, D., Hogg, D. W., Lang, D., & Goodman, J. 2013, PASP, 125, 306
Fragkoudi, F., Di Matteo, P., Haywood, M., et al. 2018, A&A, 616, A180
Frankel, N., Sanders, J., Rix, H.-W., Ting, Y.-S., & Ness, M. 2019, ApJ, 884, 99
Fuhrmann, K. 2011, MNRAS, 414, 2893
García Pérez, A. E., Allende Prieto, C., Holtzman, J. A., et al. 2016, AJ, 151, 144
García Pérez, A. E., Ness, M., Robin, A. C., et al. 2018, ApJ, 852, 91
Gavazzi, G., Consolandi, G., Dotti, M., et al. 2015, A&A, 580, A116
Genovali, K., Lemasle, B., Bono, G., et al. 2014, A&A, 566, A37
Gonzalez, O. A., Rejkuba, M., Zoccali, M., et al. 2013, A&A, 552, A110
Gunn, J. E., Siegmund, W. A., Mannery, E. J., et al. 2006, AJ, 131, 2332
Harris, C. R., Millman, K. J., van der Walt, S. J., et al. 2020, Natur, 585, 357

Hasselquist, S., Shetrone, M., Cunha, K., et al. 2016, ApJ, 833, 81
Hayden, M. R., Holtzman, J. A., Bovy, J., et al. 2014, AJ, 147, 116
Hayes, C. R., Masseron, T., Sobeck, J., et al. 2022, ApJS, 262, 34
Hill, V., Lecureur, A., Gómez, A., et al. 2011, A&A, 534, A80
Hilmi, T., Minchev, I., Buck, T., et al. 2020, MNRAS, 497, 933
Holtzman, J. A., Harrison, T. E., & Coughlin, J. L. 2010, AdAst, 2010, 193086
Horta, D., Schiavon, R. P., Mackereth, J. T., et al. 2021, MNRAS, 500, 1385
Hunter, J. D. 2007, CSE, 9, 90
Imig, J., Price, C., Holtzman, J. A., et al. 2023, ApJ, 954, 124
Iwamoto, K., Brachwitz, F., Nomoto, K., et al. 1999, ApJS, 125, 439
Johnson, C. I., Rich, R. M., Simion, I. T., et al. 2022, MNRAS, 515, 1469
Johnson, J. W., Weinberg, D. H., Blanc, G. A., et al. 2025, ApJ, 988, 8
Joshi, Y. C., Deepak, & Malhotra, S. 2024, FrASS, 11, 1348321
Kemp, A. J., Casey, A. R., Miles, M. T., et al. 2018, MNRAS, 480, 1384
Khoperskov, S., Di Matteo, P., Steinmetz, M., et al. 2025, A&A, 700, A90
Kirby, E. N., Xie, J. L., Guo, R., et al. 2019, ApJ, 881, 45
Kobayashi, C., & Nakasato, N. 2011, ApJ, 729, 16
Kobayashi, C., Umeda, H., Nomoto, K., Tominaga, N., & Ohkubo, T. 2006, ApJ, 653, 1145
Kubryk, M., Prantzos, N., & Athanassoula, E. 2015, A&A, 580, A127
Lee, Y. H., Ann, H. B., & Park, M.-G. 2019, ApJ, 872, 97
Li, C., & Zhao, G. 2017, ApJ, 850, 25
Li, Z., Cai, Z., Wang, X., et al. 2025, ApJS, 280, 62
Lugaro, M., Herwig, F., Lattanzio, J. C., Gallino, R., & Straniero, O. 2003, ApJ, 586, 1305
Magrini, L., Viscasillas Vázquez, C., Spina, L., et al. 2023, A&A, 669, A119
Majewski, S. R., Schiavon, R. P., Frinchaboy, P. M., et al. 2017, AJ, 154, 94
Martig, M., Minchev, I., Ness, M., Fouesneau, M., & Rix, H.-W. 2016, ApJ, 831, 139
Masseron, T., Merle, T., Hawkins, K., et al. 2016, BACCHUS: Brussels Automatic Code for Characterizing High accUracy Spectra, Astrophysics Source Code Library, ascl:1605.004
McWilliam, A., Piro, A. L., Badenes, C., & Bravo, E. 2018, ApJ, 857, 97
McWilliam, A., & Rich, R. M. 1994, ApJS, 91, 749
McWilliam, A., & Zoccali, M. 2010, ApJ, 724, 1491
Menéndez-Delmestre, K., Sheth, K., Schinnerer, E., Jarrett, T. H., & Scoville, N. Z. 2007, ApJ, 657, 790
Miglio, A., Chiappini, C., Mackereth, J. T., et al. 2021a, A&A, 645, A85
Miglio, A., Girardi, L., Grundahl, F., et al. 2021b, ExA, 51, 963
Minchev, I., Anders, F., Recio-Blanco, A., et al. 2018, MNRAS, 481, 1645
Minchev, I., Chiappini, C., & Martig, M. 2014, A&A, 572, A92
Minchev, I., Matijevic, G., Hogg, D. W., et al. 2019, MNRAS, 487, 3946
Minelli, A., Mucciarelli, A., Romano, D., et al. 2021, ApJ, 910, 114
Minniti, D., Olszewski, E. W., Liebert, J., et al. 1995, MNRAS, 277, 1293
Miranda, M. S., Pilkington, K., Gibson, B. K., et al. 2016, A&A, 587, A10
Montalbán, J., Mackereth, J. T., Miglio, A., et al. 2021, NatAs, 5, 640
Myers, N., Donor, J., Spoo, T., et al. 2022, AJ, 164, 85
Nair, P. B., & Abraham, R. G. 2010, ApJL, 714, L260
Nandakumar, G., Ryde, N., Schultheis, M., et al. 2025, ApJL, 982, L14
Nepal, S., Chiappini, C., Pérez-Villegas, A., et al. 2026, A&A, 707, A190
Ness, M., Freeman, K., Athanassoula, E., et al. 2013, MNRAS, 430, 836
Ness, M., & Lang, D. 2016, AJ, 152, 14
Nidever, D. L., Holtzman, J. A., Allende Prieto, C., et al. 2015, AJ, 150, 173
Otto, J. M., Frinchaboy, P. M., Myers, N. R., et al. 2026, AJ, 171, 91
Palla, M., Magrini, L., Spitoni, E., et al. 2024, A&A, 690, A334
Pandey, A., & Gerhard, O. 2025, MNRAS, 542, 1969
Prantzos, N., Abia, C., Chen, T., et al. 2023, MNRAS, 523, 2126
Prantzos, N., Abia, C., Cristallo, S., Limongi, M., & Chieffi, A. 2020, MNRAS, 491, 1832
Prantzos, N., Abia, C., Limongi, M., Chieffi, A., & Cristallo, S. 2018, MNRAS, 476, 3432
Prantzos, N., Charbonnel, C., & Iliadis, C. 2017, A&A, 608, A28
Queiroz, A. B. A., Anders, F., Chiappini, C., et al. 2020, A&A, 638, A76
Queiroz, A. B. A., Anders, F., Santiago, B. X., et al. 2018, MNRAS, 476, 2556
Queiroz, A. B. A., Chiappini, C., Perez-Villegas, A., et al. 2021, A&A, 656, A156
Ratcliffe, B., Minchev, I., Anders, F., et al. 2023, MNRAS, 525, 2208
Ratcliffe, B. L., & Ness, M. K. 2023, ApJ, 943, 92
Razera, R., Barbuy, B., Moura, T. C., et al. 2022, MNRAS, 517, 4590
Recio-Blanco, A., de Laverny, P., Kordopatis, G., et al. 2014, A&A, 567, A5
Reichert, M., Obergaulinger, M., Aloy, M. Á., et al. 2023, MNRAS, 518, 1557
Reichert, M., Obergaulinger, M., Eichler, M., Aloy, M. Á., & Arcones, A. 2021, MNRAS, 501, 5733
Rich, R. M., Origlia, L., & Valenti, E. 2007, ApJL, 665, L119
Rix, H.-W., Chandra, V., Andrae, R., et al. 2022, ApJ, 941, 45
Rodríguez, Ó., Maoz, D., & Nakar, E. 2023, ApJ, 955, 71
Rojas-Arriagada, A., Recio-Blanco, A., de Laverny, P., et al. 2017, A&A, 601, A140
Rojas-Arriagada, A., Zoccali, M., Schultheis, M., et al. 2019, A&A, 626, A16
Rosas-Guevara, Y., Bonoli, S., Puchwein, E., Dotti, M., & Contreras, S. 2025, A&A, 698, A20
Ryde, N., Nandakumar, G., Schultheis, M., et al. 2025, ApJ, 979, 174
Sales-Silva, J. V., Cunha, K., Smith, V. V., et al. 2024, ApJ, 965, 119
Sales-Silva, J. V., Daflon, S., Cunha, K., et al. 2022, ApJ, 926, 154
Santiago, B. X., Brauer, D. E., Anders, F., et al. 2016, A&A, 585, A42
Schiavon, R. P., Phillips, S. G., Myers, N., et al. 2024, MNRAS, 528, 1393
Schönrich, R., & McMillan, P. J. 2017, MNRAS, 467, 1154
Seitenzahl, I. R., Ciaraldi-Schoolmann, F., Röpke, F. K., et al. 2013, MNRAS, 429, 1156
Sestito, F., Venn, K. A., Arentsen, A., et al. 2023, MNRAS, 518, 4557
Sit, T., Weinberg, D. H., Wheeler, A., et al. 2024, ApJ, 970, 180
Smartt, S. J., Venn, K. A., Dufton, P. L., et al. 2001, A&A, 367, 86
Smith, M. C., Evans, N. W., Belokurov, V., et al. 2009, MNRAS, 399, 1223
Smith, V. V., Bizyaev, D., Cunha, K., et al. 2021, AJ, 161, 254
Spina, L., Magrini, L., & Cunha, K. 2022, Univ, 8, 87
Spina, L., Ting, Y. S., De Silva, G. M., et al. 2021, MNRAS, 503, 3279
Stanghellini, L., & Haywood, M. 2018, ApJ, 862, 45
Steinmetz, M., Guiglion, G., McMillan, P. J., et al. 2020, AJ, 160, 83
Sun, W., Shen, H., Jiang, B., & Liu, X. 2024, ApJS, 272, 8
Thielemann, F. K., Eichler, M., Panov, I. V., & Wehmeyer, B. 2017, ARNPS, 67, 253
Tripodi, R., D'Eugenio, F., Maiolino, R., et al. 2024, A&A, 692, A184
Troncoso, P., Maiolino, R., Sommariva, V., et al. 2014, A&A, 563, A58
Vasiliev, E., & Baumgardt, H. 2021, MNRAS, 505, 5978
Ventura, P., D'Antona, F., Di Criscienzo, M., et al. 2012, ApJL, 761, L30
Virtanen, P., Gommers, R., Oliphant, T. E., et al. 2020, NatMe, 17, 261
Wang, K., Carrillo, A., Ness, M. K., & Buck, T. 2024, MNRAS, 527, 321
Wang, X., Jones, T., Vulcani, B., et al. 2022, ApJL, 938, L16
Watson, D., Hansen, C. J., Selsing, J., et al. 2019, Natur, 574, 497
Wegg, C., & Gerhard, O. 2013, MNRAS, 435, 1874
Wheeler, J. C., Cowan, J. J., & Hillebrandt, W. 1998, ApJL, 493, L101
Willett, E., Miglio, A., Mackereth, J. T., et al. 2023, MNRAS, 526, 2141
Wilson, J. C., Hearty, F. R., Skrutskie, M. F., et al. 2019, PASP, 131, 055001
Winteler, C., Käppeli, R., Perego, A., et al. 2012, ApJL, 750, L22
Woosley, S. E., & Weaver, T. A. 1995, ApJS, 101, 181
Zasowski, G., Schultheis, M., Hasselquist, S., et al. 2019, ApJ, 870, 138
Zoccali, M., Hill, V., Lecureur, A., et al. 2008, A&A, 486, 177
Zoccali, M., Vasquez, S., Gonzalez, O. A., et al. 2017, A&A, 599, A12